

Reconfigurable Memory Distribution Network for Parallel Computing Systems

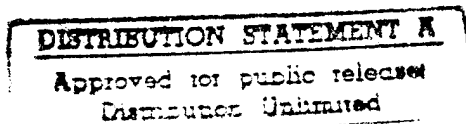
N00014-91J-1618



FINAL REPORT

for

William B. Miceli
ONR Code 4414
Office of Naval Research
800 North Quincy Street
Arlington, Virginia 22217-5660



DTIC COPY AVAILABLE

Principal Investigators: Sing H. Lee, Y. Fainman, and V.H. Ozguz

19950922 074

Table of Contents

	pages
Abstract	1
I. Statement of the problem	2
II. Program goal	2
III. Technical approach	3
IV. Accomplishments	4
4.1. Optical components development	5
4.1.1. Near infrared photorefractive LiNbO ₃	5
4.1.2. Photorefractive holographic lens array analysis	6
4.1.3. Wavelength multiplexed photorefractive lens array	7
4.2. Electronic chip development	9
4.3. Automated exposure system	10
4.4. MDN system demonstration	12
4.4.1. System construction	12
4.4.2. Application demonstration - parallel database search	13
V. Conclusion and future work	16
VI. List of publications resulted from the research carried out in this contract/grant	17
Appendix A. Characterization of argon annealed and Nd doped LiNbO ₃ at near infrared wavelength	18
Appendix B. Geometric analysis on holographic lens array	23
Appendix C. Diffraction analysis of photorefractive holographic lenses	26
Appendix D. Photorefractive lens array image system design optimization	37
Appendix E. Wavelength-multiplexed reconfigurable interconnect using a volume holographic lens array	40
Appendix F. Memory distribution network system description	44
Appendix G. Application demonstration - parallel data base search	50

Abstract

The objective of the program is to develop a Memory Distribution Network (MDM) for parallel access to secondary storage (devices) for high performance computing. The secondary storage was a large page oriented memory. It was to be connected to a smaller array of electronic processors for information retrieval. We have designed and constructed a novel reconfigurable interconnection scheme that allows a 4x4 arrays of 32x32 bits page oriented optical memory be parallel accessed with five different interconnection topologies using wavelength tuning. We have also designed, fabricated and tested the MOSIS chips that would process pages of 32x32 bits information received from the large memory before transferring the processed information to the smaller array of electronic processors. The system was capable of operating at 10 MHz with a memory retrieval throughput of 10^4 Mbits/sec. We have also demonstrated the application of parallel database search on the MDN system.

Accession For	
NTIS CRA&I	<input checked="checked" type="checkbox"/>
DTIC TAB	<input type="checkbox"/>
Unannounced	<input type="checkbox"/>
Justification	
By <i>Perlti</i>	
Distribution /	
Availability Codes	
Dist	Avail and/or Special
A-1	

I. Statement of the Problem

Technologies for storing information optically is advancing to 3D parallel access optical memory, such as volume hologram, spectral hole burning, and 2-photon based memories. All of these technologies rely on page-oriented, parallel readout of the memory with a space-bandwidth product on the order of 10^6 or larger. However, the array size of parallel opto-electronic or arbitrary electronic processing element (APE) array is usually less than 10^3 due to the limitation of electronic CMOS fabrication. A physical as well as logical size mismatch exists between the parallel access optical memory and the APE array. Therefore, a novel optical interconnection technology is required to interface between memory and APE array. In general, we would like to be able to access any bit of information from the recalled memory page by any processor in the APE array. However, many applications require each APE to access only limited sub-array in the recalled memory page. To support such applications, the interface should be constructed allowing each APE with full connectivity to a sub-array of the memory.

II. Program Goal

The goal of this project is to develop a Memory Distribution Network (MDN) for parallel access secondary storage devices for high performance computing. To accomplish this goal, we will develop a free-space reconfigurable interconnect system for achieving interconnects between memory and APE array and to develop a memory interconnection processors (MIPs) using opto-electronic integrated circuits for preprocessing the information from the memory.

The MDN system should be demonstrated with the following specific technological objectives. The MIPs will be designed and constructed to interconnect a 16×16 array of APEs with 16×16 bit plane-oriented parallel access optical memory where the size of the accessible sub-array will be 4×4 . The system will be designed to operate with interconnection speed of 30kHz and to retrieve from the memory 256 Mbit/sec. The memory will allow storage of 32 bit planes, each of 16×16 bits. The memory access time will be designed to provide the necessary throughput of 256 Mbit/sec. Application of database search or image processing where massive amounts of data have to be processed in parallel will be demonstrated using our MDN system.

III. Technical Approach

To accomplish the program goal, our technical approach was set as follows: (1) semi space-variant optical interconnect to image memory sub-fields to the desired locations on the MIPS via a holographic lens array; (2) wavelength multiplexed lens array to achieve reconfigurable interconnects; (3) an array of MIPS to do preprocess.

Fig.1 shows the schematic diagram of our approach. A holographically multiplexed lens array in conjunction with a MIP array is used to distribute the data from a mass parallel memory to a parallel processing array. Selecting different lenslets allows the routing of portions (sub-fields) of the large (10^6) bit plane memory pages to the appropriate optoelectronic MIPS. The MIPS then select the requested information from the memory sub-field and forward them to the PEs that requested them. Different sub-field of the selected memory page can be routed to different MIPS by tuning the wavelength of illumination. This allows us to select at run time among several sets of interconnections (e.g. shifting, broadcasting, etc.).

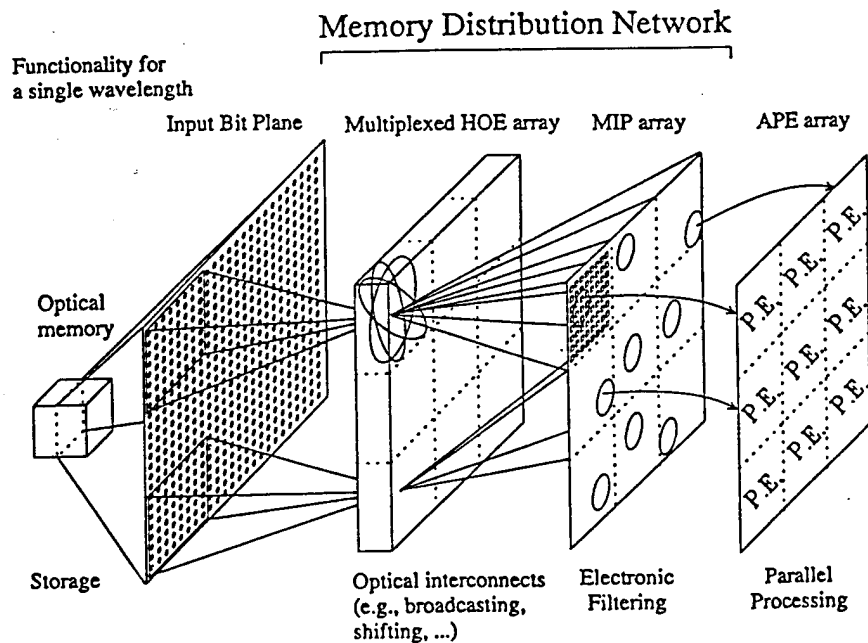


Fig.1. Schematic diagram of the Memory Distribution Network.

Our approach towards optical interconnection is unique in several aspects: (1) It requires much fewer interconnect stage than the other approaches for multistage interconnection network. For m multiplexed lenses in a crystal volume, the number of stages is reduced by a factor of $m/2$. (2) It can accommodate parallel broadcasting and permutations of many data channels (e.g., 64 bits) rather than single bit wide channels. (3) Given sufficient storage capacity in the crystals so that many multiplexed lenslets can be stored, our MDN approach can implement a variety of architectures (regular as well as irregular, existing or future interconnect architectures). (4) The using of MIPs provides additional programmability (in electronics) combined with the programmability of HOE to support efficient memory distribution.

VI. Accomplishments

The MDN project was accomplished with the performance better than the original program goal specification except that MIP array size was 8×8 instead of 16×16 due to the cost consideration; however, the result can be extended to large size. The MDN system was designed, constructed, and implemented using a novel wavelength multiplexed volume holographic lens array. We have demonstrated parallel access of a 32×32 bit page-oriented optical memory with 5 different interconnect topologies using wavelength reconfiguration. The system was designed to operate at 10MHz with a memory retrieving throughput of 10^4 Mbit/sec. An 8×8 MIP array was designed, and it was integrated into the MDN system. Application of parallel database search was demonstrated on the MDN system.

The accomplishments for the MDN project can be summarized into four parts: optical components development, electronic chip development, automated exposure system construction, and MDN system demonstration. For optical components development, we have explored and characterized a new type of LiNbO_3 photorefractive crystal that is sensitive in near infrared (NIR) wavelength; we have also fabricated wavelength multiplexed holographic lens array in this NIR crystal and characterized its performance. For electronic chip development, we have designed and tested two chips fabricated through MOSIS. MIP functions were implemented on the chips. For reducing the fabrication cost, we have constructed an automated exposure system which is capable of fabricating wavelength multiplexed lens array for arbitrary interconnect architectures. For MDN system demonstration, we integrated the MOSIS MIP chip into the MDN

system and demonstrated parallel database search application. The detailed report on the accomplishments is in the following.

4.1. Optical Components Development

4.1.1. Near Infrared Photorefractive LiNbO₃

High power semiconductor lasers are operating at NIR wavelength; however, there are very few existing holographic materials sensitive to NIR spectrum. The dichromated gelatin, photopolymers (Dupont's and Polaroid's), as well as most ferroelectric photorefractive materials cannot record holograms in NIR. We have explored the possibility of recording holograms at NIR in photorefractive lithium niobate that was specially treated. We found that an argon annealed 0.1% (mole) Fe doped LiNbO₃ provided by Prof. Liang-Ying Xu of the Shanghai Institute of Ceramics has good sensitivity in NIR. We have characterized such a sample, for recording the wavelength multiplexed lens array necessary for our approach to MDN.

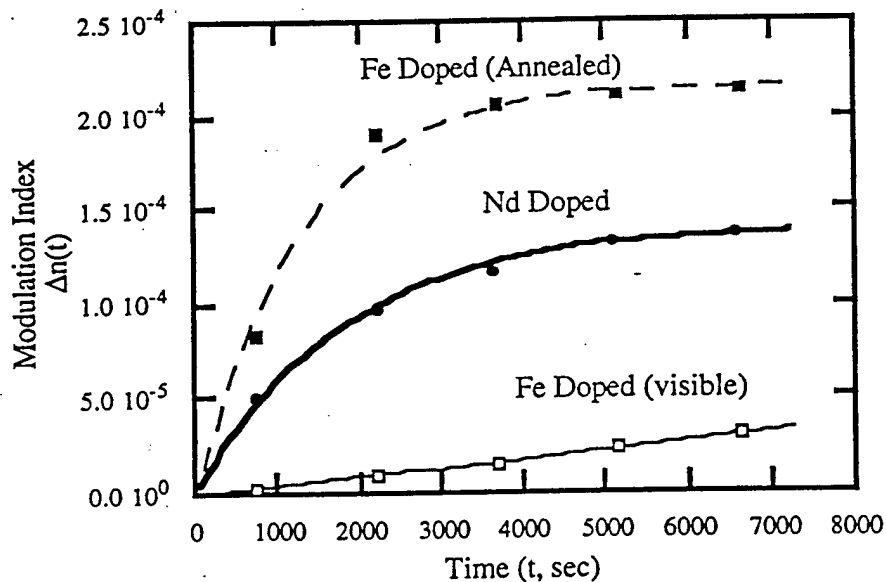


Fig.2 Comparison of holographic recording dynamics at 790 nm for three different LiNbO₃ samples.

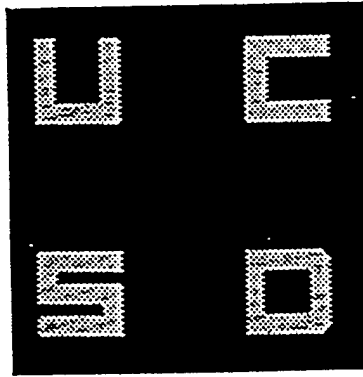


Fig.3. Image formed by a 2x2 photorefractive lens array

Using a tunable Titanium Sapphire laser, three important characteristics of the material can be evaluated: the sensitivity of the material, the saturation efficiency of the material, and the wavelength separation between multiplexed holograms. To appreciate the improvement in NIR sensitivity of that sample from the Shanghai Institute of Ceramics demonstrates over a standard doping of lithium niobate (Crystal Technology), Fig.2 compares the writing dynamics of the two samples at 790 nm. It can be seen that Shanghai Institute of Ceramics sample records much faster than the Crystal Technology sample. The sensitivity of the Shanghai Institute of Ceramics is $5 \times 10^{-7} \text{ cm}^3/\text{J}$. The saturation efficiency of a 1 mm thick hologram is 40% (including absorption). The wavelength selectivity of this 1 mm was measured to be 0.15 nm. This indicates that holograms can be stored as close as 0.3 nm apart. Allowing for many configurations of the lens array to be superimposed using a laser with a relatively short tuning range. See Appendix A for more detailed information.

4.1.2. Photorefractive Holographic Lens Array Analysis

The lens array was analyzed using geometric and diffractive optical techniques to determine the appropriate design. The geometric analysis determined the effects of off-axis imaging on the spot size and distortion of the image. The diffraction analysis determined the diffraction limited spot size and the Bragg limited field of view. The Bragg limited field of view is an effect that reduces the size of an image due to the angular selectivity of a volume holographic lens. If an off-axis lens is recorded, the size of the image from that lens is inversely proportional to the distance off-axis of the image. By combining these two effects, an optimum design could be achieved. Given other constraints in the construction of the system, the optimum design was to use a lens array with a focal length of 40 mm and a lens size of 2 mm. With this design, lenses in the

array could redirect portions of the input image to 25 possible (non-overlapping) destinations and still retain a 2 mm field of view. A larger number of destinations could be achieved by reducing the field of view. The predicted spot size for this design was diffraction limited at 32 microns. Fig.3 shows an image formed by a 2x2 photorefractive lens array. See Appendix B for more detailed information on geometric analysis, Appendix C on diffraction analysis; and Appendix D on design optimization.

4.1.3. Wavelength Multiplexed Photorefractive Lens Array

The lens array was tested independently of the chip to verify its performance before integrating with the MIP chip. Several prototype lens arrays were fabricated using a custom automated exposure system. A 4 x 4 lens array was recorded in the NIR sensitive photorefractive LiNbO₃ sample mentioned in Section 5.1.1 and Appendix A with five separate configurations of the lens array interconnect stored in the crystal (i.e. five lens arrays were wavelength multiplexed). The lens array was tested using the optical system diagrammed in Fig.4. The vertical polarized input image enters a polarizing beam splitter and reflects toward a quarter-wave plate. The image is then right-hand circularly polarized when it strikes the holograms in LiNbO₃. The reflection from the holograms then passes through the quarter-wave plate and is horizontally polarized, allow it to pass through the beam-splitter and be imaged to a CCD camera.

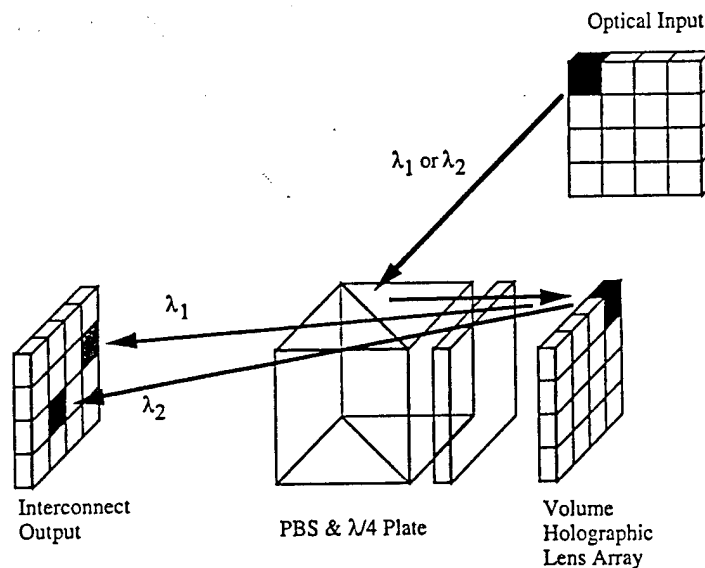


Fig.4. Optical system for implementing a reconfigurable semi-space-variant interconnect.

The following performance criteria were evaluated: spot size, field of view, efficiency, wavelength separation, and crosstalk. The spot size was measured to be 38 microns, close to the predicted design value. The field of view was undistorted at a full 2 mm. Off-axis lenses were used to further evaluate the field of view. Image shifting of over 2.8 mm was achieved without reduction in field of view. For 1 mm images, a maximum image shift of 5.6 mm was measured. The efficiency of each holographic lens was measured to be 1%. This value is significantly lower than the saturation efficiency because by multiplexing lenses, the storage capacity of the hologram is divided between each hologram. The wavelength separation was 0.4 nm to 1.0 nm. This was a result of limitations in the illumination source. Even with the lenses that were separated by 0.4 nm the crosstalk from the stored holograms was less than 0.4% of the signal of the primary reconstruction. Crosstalk from lenses adjacent in the array was less than 4% of the primary reconstruction. Fig.5 shows 5 different interconnect topologies implemented by a 4x4 wavelength multiplexed lens array. See Appendix E for more detailed information.

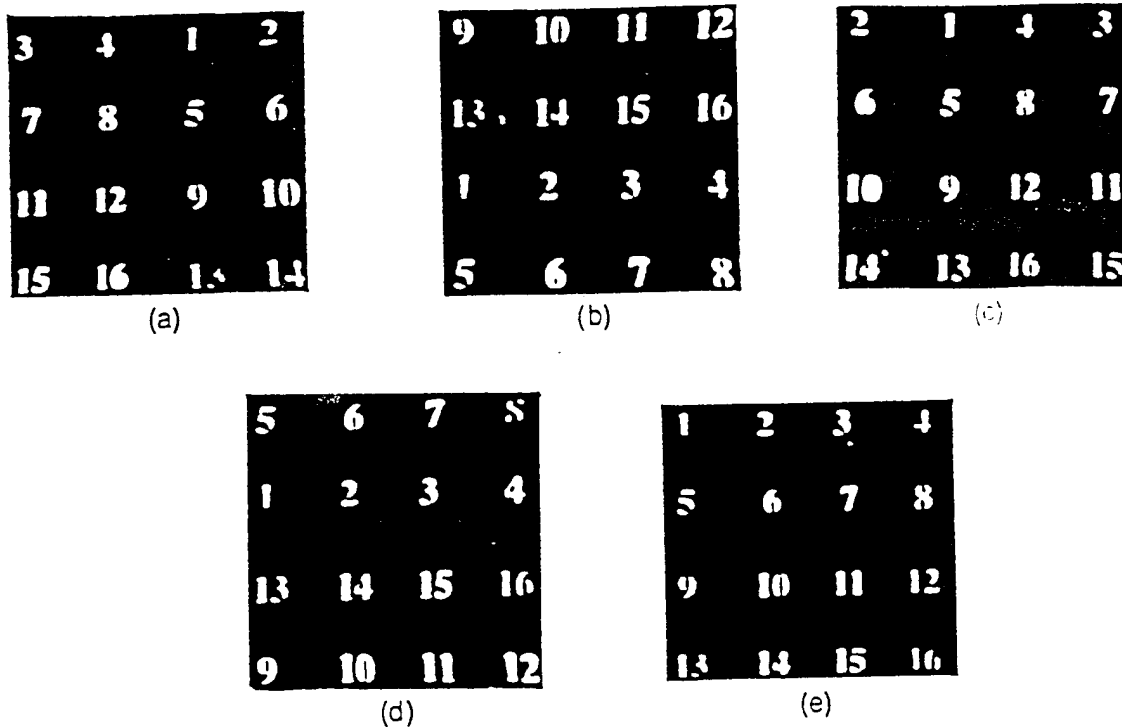


Fig.5. Different interconnect topologies implemented by a 4x4 wavelength multiplexed lenses array. (a) Vertical half-fold (stage 1: $\lambda = 799.8$ nm), (b) horizontal half-fold (stage 2: $\lambda = 796.6$ nm), (c) vertical quarter-fold (stage 3: $\lambda = 801.1$ nm), (d) horizontal quarter-fold (stage 4: $\lambda = 798.2$ nm), (e) straight-through interconnect (stage 5: $\lambda = 798.8$ nm).

4.2. Electronic Chip Development

Two electronic "Tiny" chips are fabricated through MOSIS, implementing a MIP element in CMOS 2 micron technology. The first chip (see Fig.6) implements a dense detector design (8 x 8 array, 125 micron spacing) with a basic bit selection circuit to test the limitations of the optical interconnect. The size of the sensitive areas of the photodetectors are 25 x 25 μm . These detectors have been characterized up to 10 MHz, showing the trade-off between sensitivity and speed at various level of optical input power. The eye diagram at 1 MHz (Fig.7) shows a good falling edge with approximately 2 μW of light power (at 830 nm, output of a laser diode) pulsed at random (50%) duty cycle and a good rising edge resulting from the precharge. They can also be operated at lower light level. A sensitivity of 0.2 μW has been demonstrated at 100 KHz.

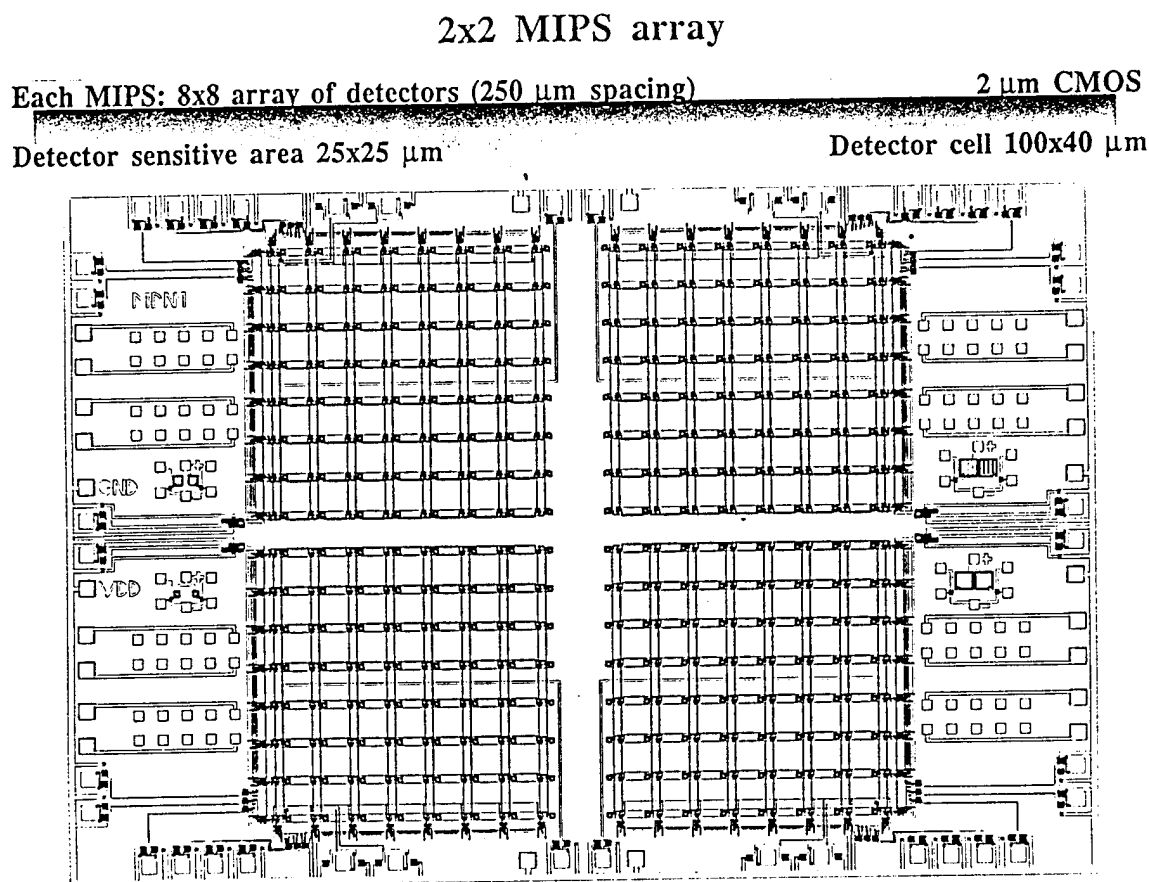


Fig.6. The first MDN's MIP chip designed with a basic bit selection circuit.

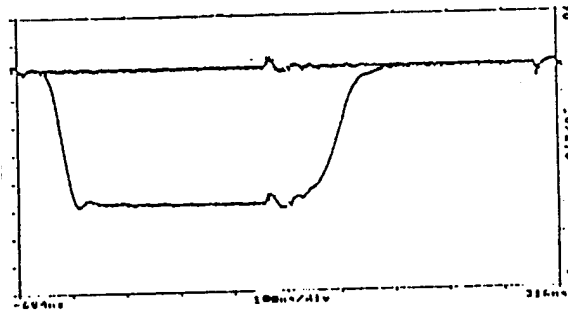


Fig.7. The eye diagram of the first MIP chip at 1MHz

The second chip (4 x 4 array, 250 micron spacing) has the additional capability of computing in parallel the Hamming distance between the 16 bit input image and a reference image (see Fig.8). A set of reference images are stored locally in the parallel shift register of each MIP element. The shift register can be loaded either from the memory side (in parallel) or from the PE side (serially). The distance is computed asynchronously by a Wallace tree of adders, more efficient for adding binary pixels than a conventional tree of adders. The execution of this computing primitive "on-the-fly" at the MIP level will alleviate the workload of the PEs in various applications (for example, pattern matching in image processing, database searching, associative memory, etc.). A PLZT modulator will be flip-chip bonded to each of the MIP elements, to provide an optical output to communicate directly with its corresponding PE in the processing array.

Since the MDN system has the capability to transmit wide (e.g., 64 bit) channels of memory, it lends itself for applications that require intensive memory access. We anticipate the current design to scale up to an array of 128 x 128 PEs. With a 64 bit wide channel per PE, this yields a cross section of 1 Mb, to be accessed at MHz frame rates. Applications that would take advantage of this capability would include template matching in image processing, database searching, associative memory, and parallel decoding of memory data to increase the capacity and reliability of the optical memory.

4.3. Automated Exposure System

In order to rapidly and efficiently expose an arbitrary wavelength multiplexed lens array, an automated exposure system was constructed. The system was based on a

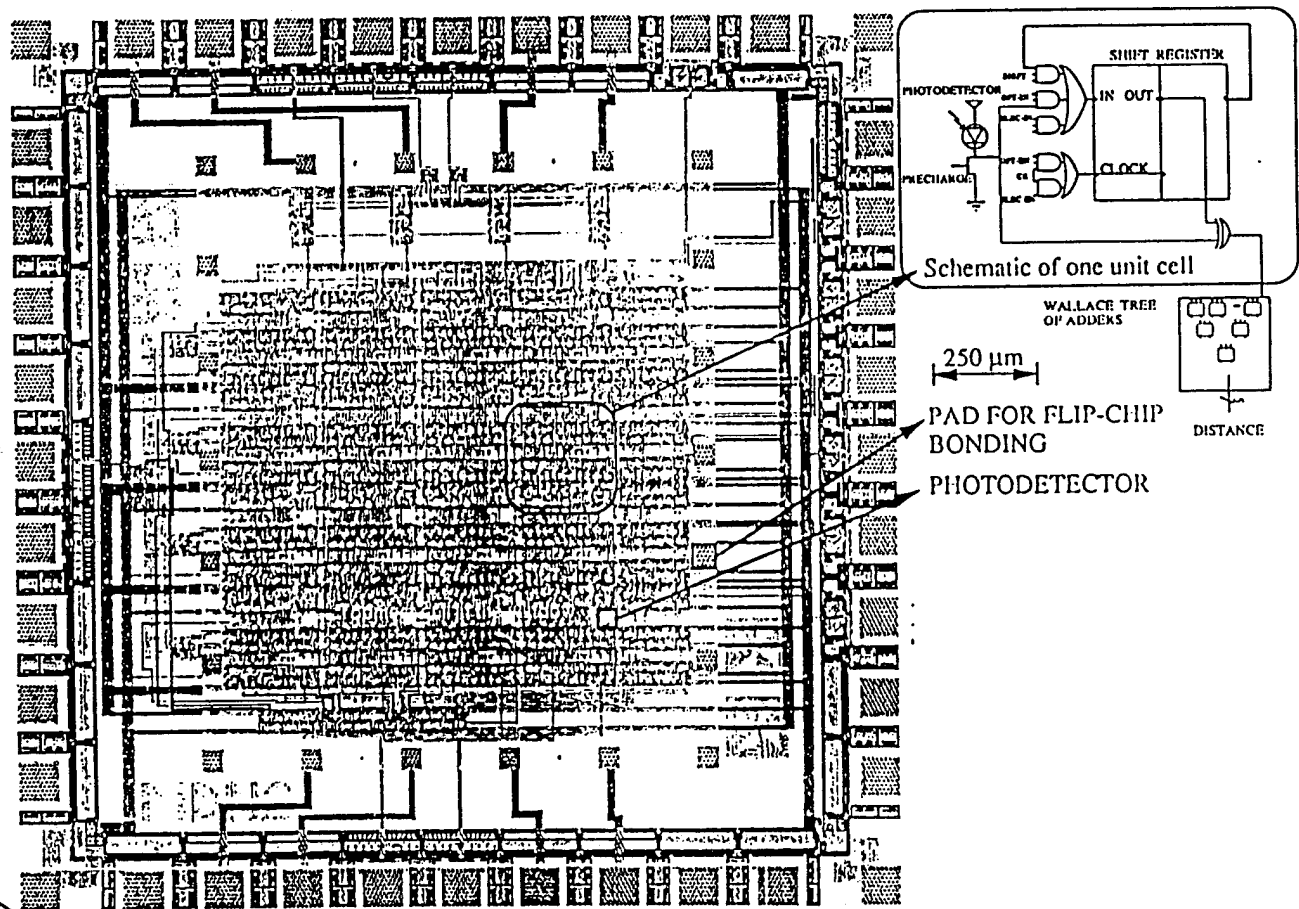


Fig.8. The second MDN's MIP chip designed with the additional capability of computing in parallel the Hamming distance between the 16 bit input image and a reference image.

computer controlled Ti:Sapphire laser and a series of computer controlled translation stages. Fig.9 shows a schematic diagram of the system. Reflection holographic lenses were recorded by two counter propagating beams. The reference beam is a fixed lens that creates a diverging point source. The object beam is produced by lens mounted on a translation stage and imaged by a 4f imaging system to the hologram plane. By moving the lens in the path of the object beam, various off-axis lens elements can be recorded in the array. An aperture is placed on each side of the holographic substrate in order to isolate a single element in the lens array for recording. The holographic material, lithium niobate, was mounted on a kinematic mount in order to reliably move the lens array between the reconstruction system and the recording system.

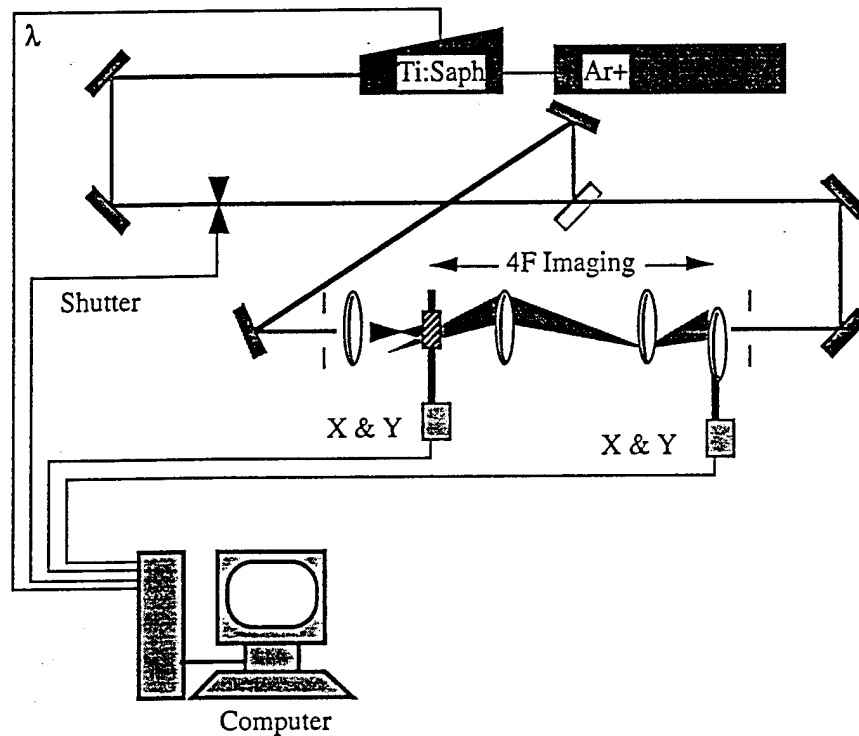


Fig.9. Automated exposure system for recording volume holographic lens array.

4.4. MDN System Demonstration

4.4.1. System Construction

A demonstration system for opto-electronic memory distribution was built and tested. The system was constructed using a tunable Ti:Sapphire laser, a fixed input memory page, the lens array and MOSIS MIP chip described previously integrated with a 486-33 MHz PC to act as the processing element. The PC could request portions of the optical memory by controlling the wavelength of the Ti:Sapphire laser. It would then receive the data via a chip tester connect directly to the MIP chip. A block diagram is provided in Fig.10. The chip was aligned to the optical interconnect to within 10 microns in the lateral direction, 130 microns along the optical axis, and to within 10 millirad rotation.

Using the MOSIS MIP chip, signals of as low as 40 nW could be detected at a rate of 1 kHz for each detector. With sufficient power, (1 MHz/ μ W) this design should be able to achieve a maximum speed of 10 MHz detection rate. By designing with a

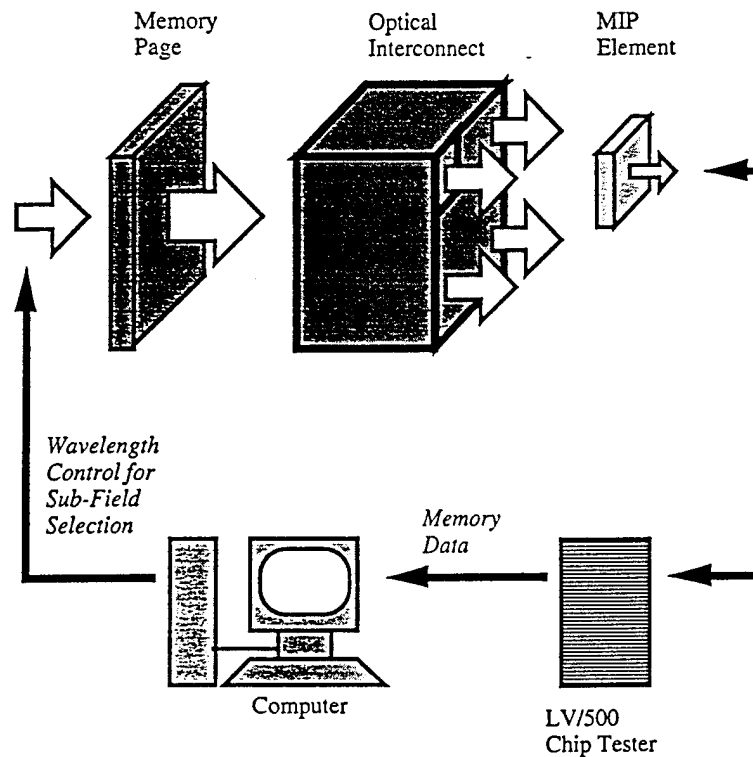


Fig.10. Block diagram of the experimental memory distribution network.

more aggressive feature size (0.8 microns), correlation, convolution, integer math functions should be possible at speeds approaching 10 MHz. See Appendix F for more detailed information.

4.4.2. Application Demonstration - Parallel Database Search

Using this prototype system, it was possible to demonstrate how a large array memory distribution network would be used to implement a parallel database search through an optical memory. Data can be encoded on a field small enough for a single element in the MIP array to read (64 pixels for this demonstration). By recording the appropriate lens array, the entire memory page can be scanned and compared with keys stored in the MIP array. Once the appropriate information is found, the results can then be transferred to a more powerful processing array.

An application based on airline travel data was developed. Data was encoded on a single page of an optical memory and presented as an input to the lens array. A host PC would request several portions of the memory page by changing the wavelength of illumination. The interconnect would reconfigure and transfer that information via the MIP chip to the host PC. The PC would then decode the data and search for specific

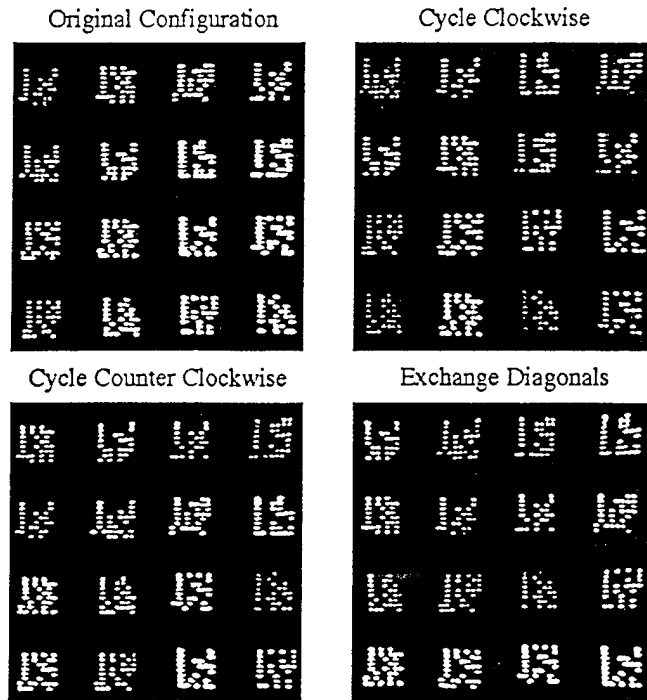


Fig.11. Four configurations of the interconnect used to demonstrate parallel search of a page oriented memory.

flight information. Fig.11 shows the reconstruction of the data page from the optical interconnect. The data requested by the PC is shown in a separate figure (Fig.12). This data is encoded in a binary format to include destination location, arrival and departure times, as well as the airline carrier. Fig.13 depicts the software application developed on the PC to interface with the memory distribution network. Notice that the output of the software application matches the data requested by the PC when wavelength 1 is used. See Appendix G for more detailed information.

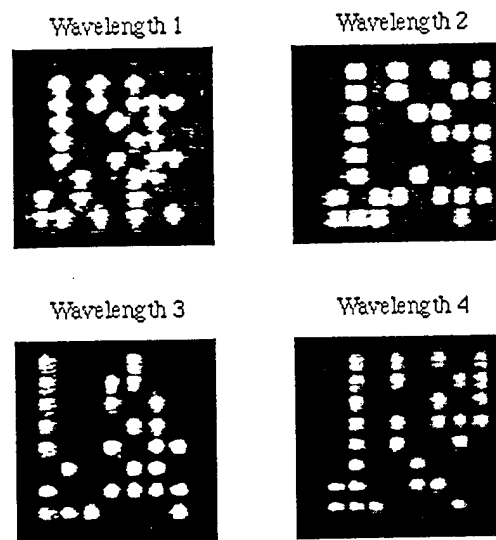


Fig.12. Data input to the MIP chip located in the upper-right corner of the low-left memory block shown in Fig.11.

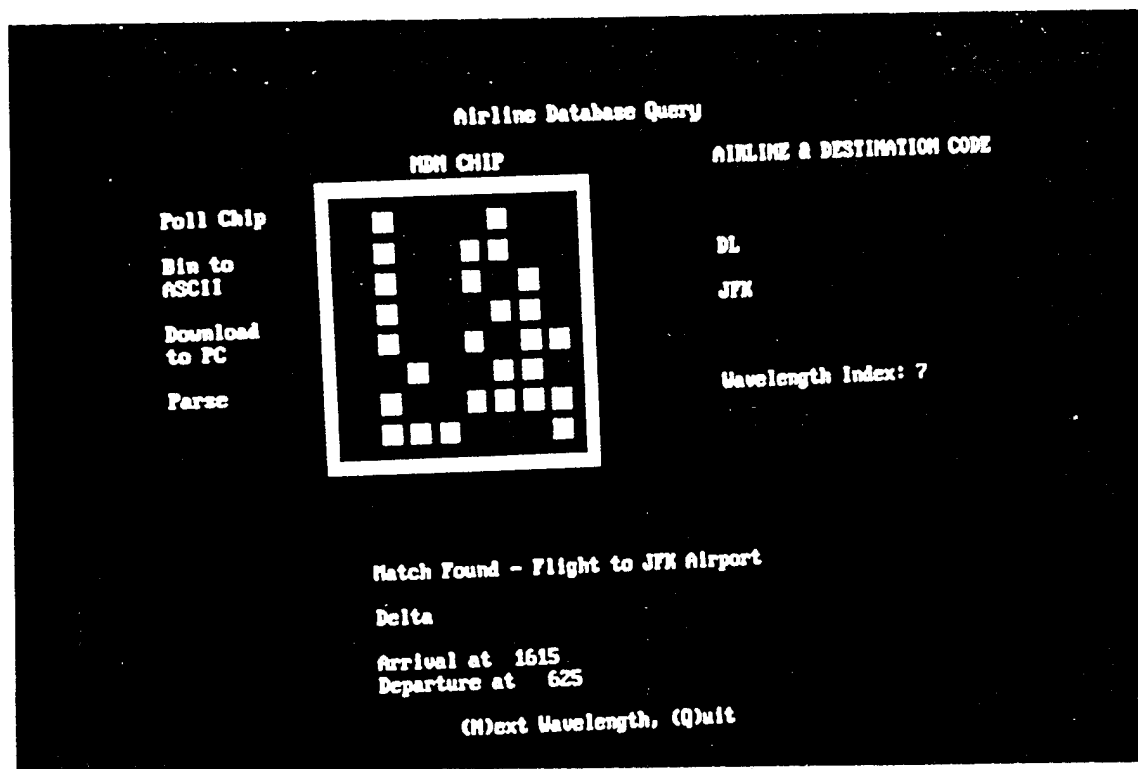


Fig.13. Software on PC to control the laser wavelength, receive the MIP chip transmission, and search entries in the database.

V. Conclusion and Future Work

The goal of the program was to investigate reconfigurable interconnect scheme for interfacing a large page-oriented optical memory to a smaller processor array as an attempt to solve the interconnect bottleneck that exist between the secondary storage and processors in high performance computing. We have successfully developed a novel reconfigurable interconnection scheme based on the use of volume holograms that are wavelength tunable and an electronic array for on-the-fly data preprocessing. We have demonstrated our concept by parallel accessing 4x4 array of a 32x32 bit page oriented optical memory with 5 different interconnection topologies. The architectural and technological characteristics of our MDN make it suitable to be assembled in compact and rugged packages.

The key technological components developed in this project, namely the combination of wavelength tunable laser diode and wavelength multiplexed volume holographic interconnects along with the interface chip, are important developments that extends beyond the scope of this project. The memory/processor interface is a subset of a more general class of interconnect problems. The solution provided by this project can be extended to other optical interconnect implementations, especially to optical interconnects between multichip modules with the built-in self-alignment capability of volume holographic optical interconnects. Hence, a broad range of applications including image processing, data base search and retrieval, where massive parallel data movements are needed, can benefit from the developed technology.

We recommend continued development on the tunable laser diode sources, materials for volume holography that are compatible with electronic manufacturing, automated exposure system for the recording of volume holograms and compact packaging concepts. Advances in these areas will keep optical interconnects as a viable technological solution to electronic interconnect problems at the chip-to-chip at the MCM level and the MCM-to-MCM on a PCB level.

VI. List of Publications Resulted from the Research Carried Out in This Contract/Grant

1. B. Catanzaro, N. Mauduit, J. Ma, Y. Fainman, S.H. Lee, "Design and demonstration of a reconfigurable semi-space variant volume holographic lens array optical interconnect", to be submitted to Applied Optics.
2. B. Catanzaro, J. Ma, Y. Fainman and S.H. Lee, "Wavelength multiplexed reconfigurable interconnect using a volume holographic lens array," Optics Letters, 1994, Vol.19, pp1358-1360.
3. J. Ma, B. Catanzaro, J.E. Ford, Y. Fainman and S.H. Lee, "Photorefractive holographic lenses and applications for dynamic focusing and dynamic image shifting," Journal of the Optical Society of America - A, 1994, Vol. 11, pp2471-2480.
4. B. Catanzaro, J. Ma, Y. Fainman, and S.H. Lee, "Wavelength multiplexed holographic lens array for optical interconnection," Proc. SPIE, 2152, 1994 (in press).
5. B. Catanzaro, J. Ma, Y. Fainman, and S.H. Lee, "Wavelength-multiplexed holographic lens array for a memory-distribution network," OSA Annual'93 Meeting at Toronto, Canada, (Oct. 1993).
6. J. Ma, B. Catanzaro, Y. Fainman, S.H. Lee, "Reflection volume holographic lenses with wide field of view and wavelength multiplexing," OSA Annual'92 Meeting at Albuquerque, N.M. (Sept. 1992).
7. B. Catanzaro, J. Ma, Y. Fainman, S.H. Lee, "Infrared wavelength multiplexed holographic storage in photorefractive Lithium Niobate," OSA Annual'92 Meeting at Albuquerque, N.M. (Sept. 1992).

Appendix A

Characterization of Argon Annealed and Nd Doped LiNbO₃ at Near Infrared Wavelength

Recent advances in developing tunable semiconductor laser arrays operating at the near infrared (0.8 μm to 1.0 μm) could support random access times to pre-stored wavelength multiplexed holograms of 100 ns, while discrete laser devices access one of twelve multiplexed holograms with a latency of 1 ns. These lasers make wavelength multiplexing a very attractive method for optical interconnection and parallel access optical memory applications. However, since very few holographic materials exhibit sensitivity at wavelengths longer than 0.7 μm , new infrared sensitive materials are needed.

We have characterized the infrared properties of three samples of c-cut LiNbO₃: 0.05% (mole) Fe doped (Crystal Technologies), argon annealed 0.1% (mole) Fe doped, and 0.05% (mole) Nd doped. The argon annealed Fe doped and Nd doped samples from the Shanghai Institute of Ceramics were grown using the Czochralski method in normal atmosphere. After poling the crystal, the Fe doped sample was annealed in an argon atmosphere at 1050°C for 10 hours. The holographic recording characterization was performed by exposing reflection holograms (which have high wavelength selectivity) with beams incident at 45° to each surface using vertical polarization. We evaluated the following figures of merit relevant to storage applications: absorption, time response, saturation value of the refractive index, energy required to write a hologram of 1% diffraction efficiency, and the photorefractive sensitivity.

We measured the absorption spectra using a 500 mW Ti:Sapphire laser (tunable from .780 to .920 microns) pumped by an Argon laser. The absorption constant for the three samples was consistently 2.3/cm for the majority of the spectrum.

Data collected on the time evolution of the diffraction efficiency was converted to the time evolution of the change in refractive index using Kogelnik's equations for absorbing phase reflection holograms.

An initial comparison was done at 790 nm because the time response of the visible doped sample is very long at longer wavelengths. Figure A1 illustrates a dramatic improvement in the time response of the argon annealed Fe doped and Nd doped samples over the standard visible Fe doped sample at 790 nm. This measurement indicates that the

full characterization of the new doping is quite important, while the visible doped sample holds little interest for recording at infrared wavelengths. For this reason, the remaining figures of merit are evaluated only for the new infrared sensitive sample.

In general, the time evolution of the refractive index modulation fit an approximation to the solution to Kukhtarev's Band Transport equations. By curve fitting the data, we determined the time response of the materials. The time response was scaled to 100 mW/cm^2 and the results are shown in Figure A2. Our curve fit also provided the saturation refractive index as a function of wavelength. These results are summarized in Figure A3. In addition, the energy required to write a 1% efficient hologram was calculated and shown in Figure A4. The photorefractive sensitivity is a measure of the strength of the hologram that can be recorded per unit of energy absorbed. Although the material is not very sensitive compared to visible recordings ($S = 10^{-3} \text{ cm}^3/\text{J}$), high sensitivity is not critical for the use of the material as a holographic lens. The sensitivity of the anneal sample is shown in Figure A5.

We have demonstrated significant sensitivity of holographic recording in LiNbO_3 to near infrared laser diode wavelengths (780 nm to 850 nm). Use at shorter wavelengths (780 nm to 800 nm) is preferable because of the faster time response and higher diffraction efficiency.

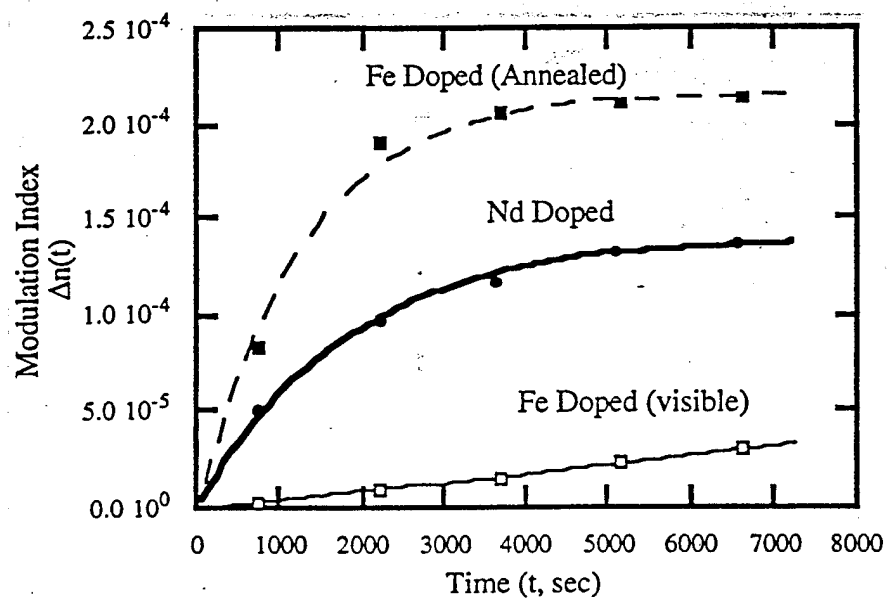


Fig.A1. Comparison of holographic recording dynamics at 790 nm for three different LiNbO₃ samples.

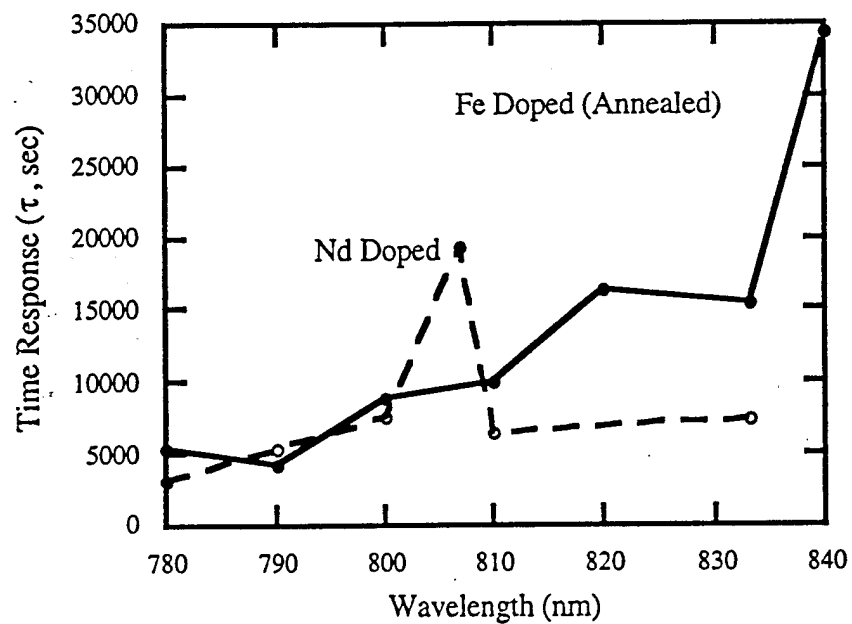


Fig.A2. Time response at 100 mW/cm² for annealed Fe-doped (0.1%) and Nd-doped (0.05%) LiNbO₃.

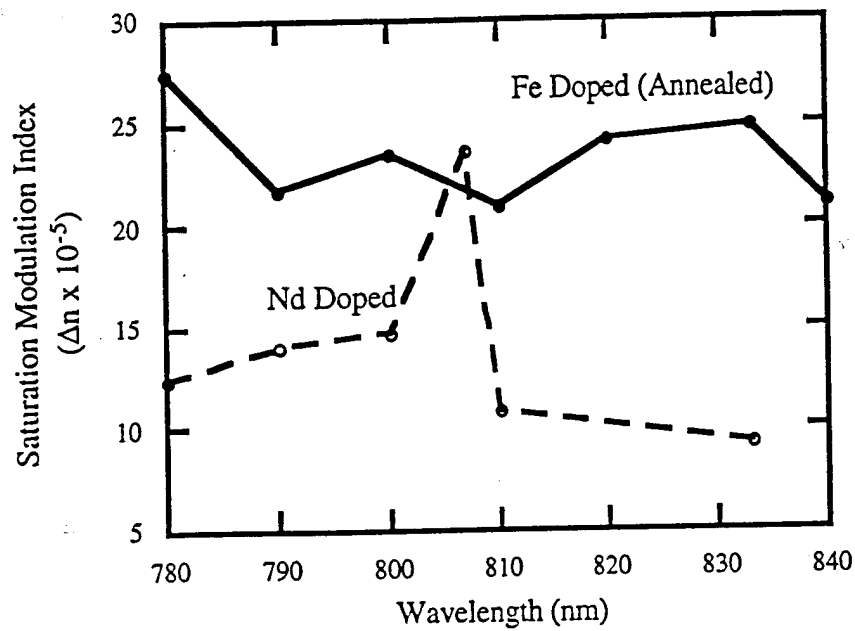


Fig.A3. Saturation modulation index for annealed Fe-doped (0.1%) and Nd-doped (0.05%) LiNbO_3 .

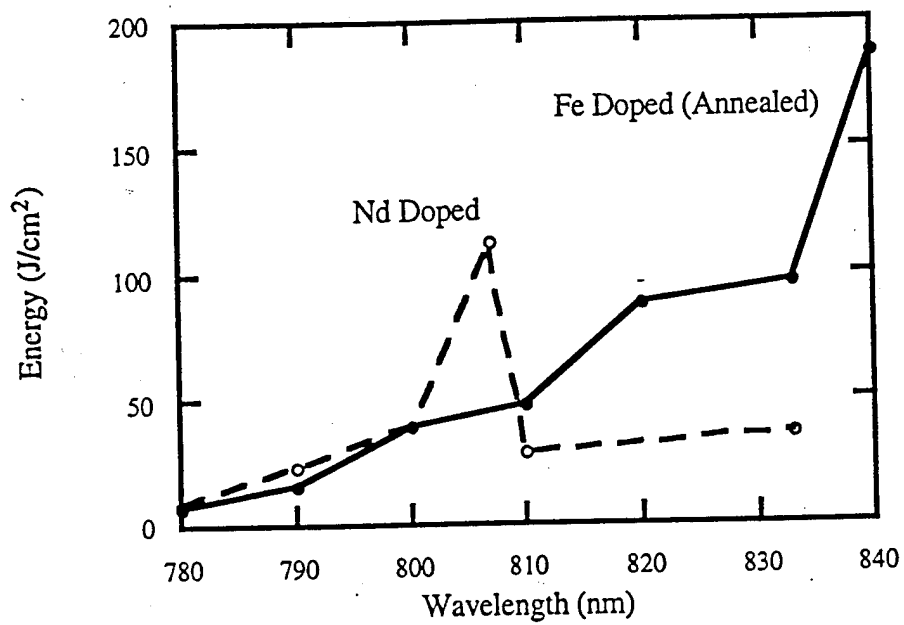


Fig.A4. Comparison of energy required to write a 1% efficient grating in annealed Fe-doped (0.1%) and Nd-doped (0.05%) LiNbO_3 .

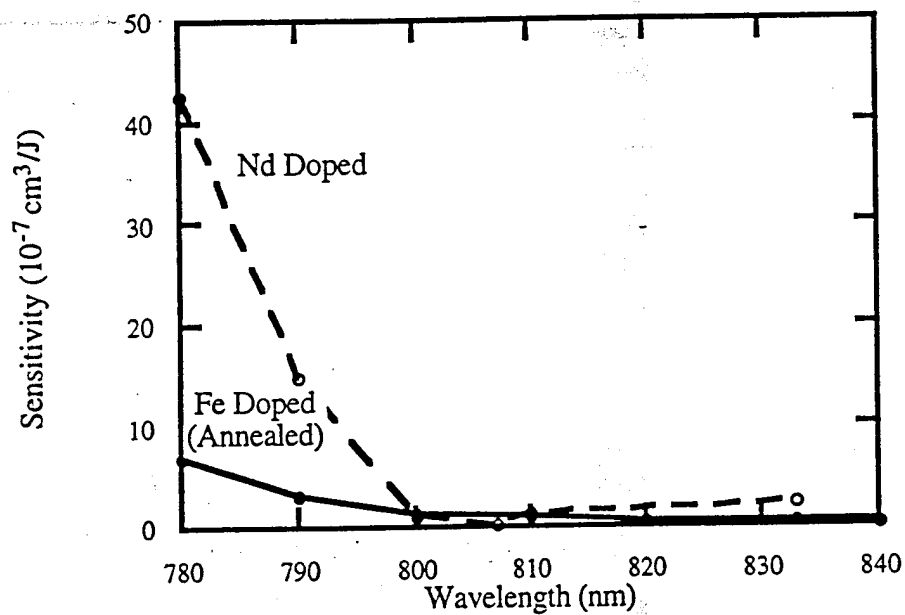


Fig.A5. Comparison of the photorefractive sensitivity for annealed Fe-doped (0.1%) and Nd-doped (0.05%) LiNbO₃ at 100 mW/cm².

Appendix B

Geometric Analysis on Holographic Lens Array

Geometric optics can play an important role in the modelling of holographic interconnects. The volume holographic lenses can be ray traced in a manner similar to refractive components. Using a commercial package, CodeV™, it was possible to simulate many similar systems to gain insight into the particular geometric optics effects that dominate the design of the lens array used in the interconnect.

The lenses were simulated as holographic elements aligned with polarization sensitive optics. The system that was simulated is diagrammed in Figure B1. Figure B2 shows a perspective view of the optical system.

Off-axis imaging in both diffractive and refractive systems can cause two problems: astigmatism and distortion. Astigmatism tends to change the shape and size of the PSF (independently of the diffraction effects from the aperture). Rays that are in the plane of the direction off-axis (tangential rays) tend to focus closer than rays that are perpendicular to the plane of the off-axis direction (sagittal rays) resulting in an elongated PSF. The distortion from off-axis imaging refers to the fact that independent of the shape of the PSF, the center-of-mass of the PSF is also displaced from the geometric prediction. Both of these phenomenon can be described analytically to some degree. Typically the astigmatism grows in proportion to x^2/f where x is the image height and f is the focal length of the lens. The distortion tends to follow a x^3 behavior. However, these effects are more easily determined by using a commercial ray-tracing program, such as CodeV™. An example of the astigmatism and distortion are shown in Figure B3 and Figure B4. The lens chosen as an example had the following specifications: $f = 40$ mm, 1 mm thick LiNbO₃, 2 mm in diameter, 15 mm off-axis image

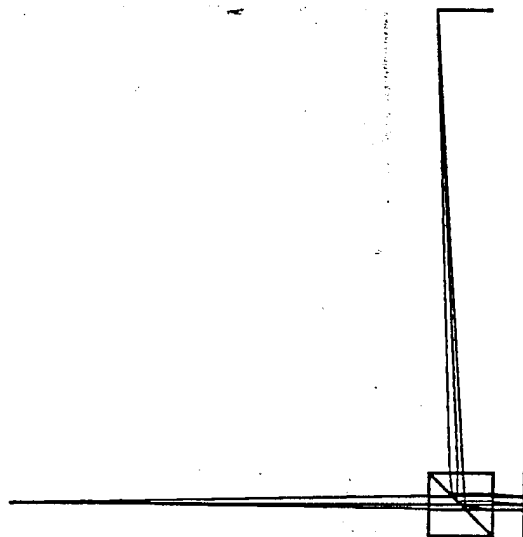


Fig.B1. System used to simulate spot sizes and distortion in the holographic lens array (generated with CodeVTM).

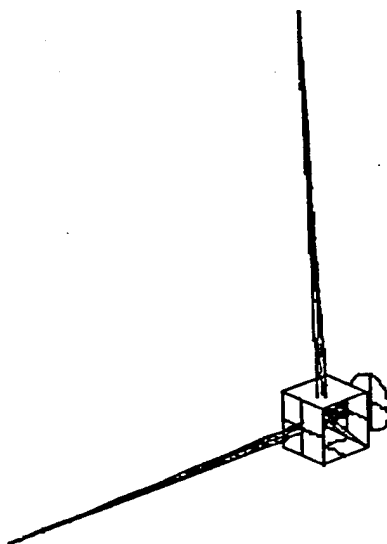


Fig.B2. Perspective view of the simulation system.

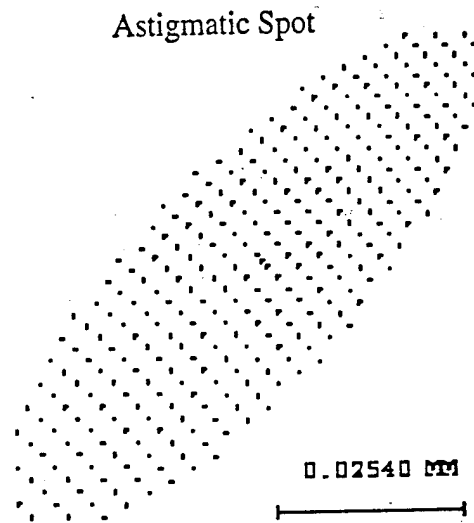


Fig.B3. Astigmatism from off-axis imaging ($f=40\text{mm}$, $d=1\text{mm}$, $D=2\text{mm}$, $x=15\text{mm}$).

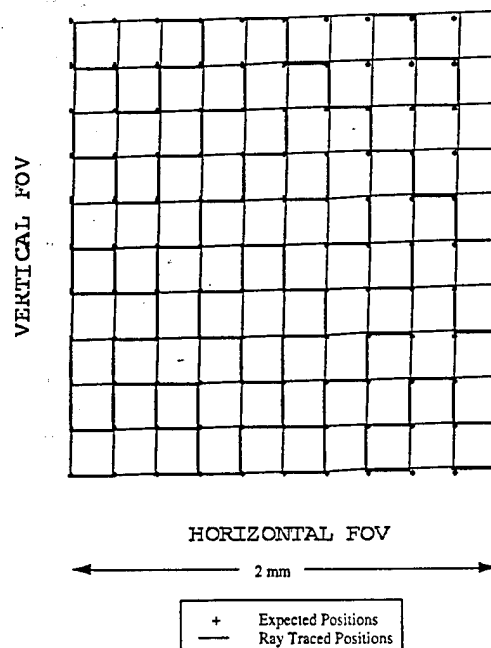


Fig.B4. Field distortion from off-axis imaging ($f=40\text{mm}$, $d=1\text{mm}$, $D=2\text{mm}$, $x=15\text{mm}$) an example had the following specifications: $f=40\text{mm}$, 1mm thick LiNbO_3 , 2mm in diameter, 15mm off-axis image.

Photorefractive holographic lenses and applications for dynamic focusing and dynamic image shifting

Jian Ma, Brian Catanzaro, Joseph E. Ford, Yeshaiah Fainman, and Sing H. Lee

Department of Electrical and Computer Engineering, University of California, San Diego, La Jolla, California 92093-0407

Received May 28, 1993; revised manuscript received March 10, 1994; accepted March 28, 1994

Wavelength-multiplexed reflective holographic lenses were recorded in a 1-mm-thick Fe-doped LiNbO₃ crystal. A simple theoretical model based on Kogelnik's coupled-wave theory and Kuktarev's photorefractive-material equations was used to characterize the photorefractive lenses in terms of Bragg-limited field of view, optimum space-bandwidth-product, and wavelength selectivity. Experimental measurement verified the theoretical calculations. An $f/3$ lens was recorded, and nearly aperture-limited diffraction performance was observed. Applications of wavelength-multiplexed photorefractive lenses were shown by demonstration of dynamic focusing and lateral image shifting.

1. INTRODUCTION

A dynamic optical imaging system is important in many applications, such as variable depth imaging in a three-dimensional memory,¹ dynamic adjustment in optical disk readers, and image shifting in global interconnections.² Dynamic focusing lenses have been investigated with the use of a liquid-crystal cell³ and the electro-optic effect.⁴⁻⁵ Both of these approaches are limited by low resolution, large f -number, and low operating speed. Another approach that was recently demonstrated uses Fourier filtering in a $4-f$ image system.¹ Although this Fourier filtering method can be operated at high speed (of the order of microseconds) with nearly diffraction-limited resolution, it is limited by the cross-talk noise, its intensive computation of the hologram, and its complicated optical system. Techniques have been proposed for dynamic image shifting by the use of birefringent prisms,⁶ flat birefringent plates,⁷ and photorefractive four-wave mixing.⁸ However, the designs that use birefringence are limited by their achievable shift, and complicated optical systems are required for shifting in both directions; the four-wave mixing approach is limited by the photorefractive response time. In this paper we demonstrate a dynamic optical imaging approach, using wavelength-multiplexed photorefractive holographic lenses. By superimposing many lenses in a single volume of holographic material, it is possible to select one of several different lenses rapidly [<1 ns (Ref. 9)] merely by tuning the wavelength. The advantages of this approach over the existing methods are (1) fast access, i.e., gigahertz; (2) system simplicity (few components), (3) ease of fabrication, and (4) flexibility: i.e., both dynamic focusing and dynamic image shifting can be achieved in a single element.

Holographic lenses have been recorded in silver halide photographic emulsions,¹⁰ dichromate gelatin films,^{11,12} and holographic photopolymer.¹³ All these materials have a very limited thickness, i.e., less than 100 μm . However, in practical applications a large thickness (several millimeters) is required for reduction of the wavelength change that is necessary for rapid selection of

stored lenses. The most serious problem associated with thick volume holographic lenses is the limited field of view originating from Bragg angular selectivity.¹⁴ For example, Syms and Solymar showed that a field of view of only 13° can be imaged by a single holographic lens recorded in a 5- μm -thick Agfa 8E56, a high-resolution photographic emulsion.¹⁴ The restriction on field of view will be much stronger if the thickness is larger than 100 μm . Our approach uses a reflection-mode hologram to achieve two features simultaneously: (1) low angular selectivity to permit a broad field of view and (2) high wavelength selectivity to permit large multiplexing and fast access. Photorefractive materials provide additional advantages of *in-situ* recording and various achievable thickness. In Section 2 we present theoretical calculations of some of the characteristics of the photorefractive lenses, such as field of view, space-bandwidth-product optimization, and wavelength selectivity based on a simplified model. In Section 3 we present the experimental results of the characterization of the lenses. In Section 4 we demonstrate the applications of wavelength-multiplexed lenses to dynamic focusing and lateral image shifting. A discussion of the issues of concern regarding practical applications is presented in Section 5, and the conclusion is presented in Section 6.

2. THEORETICAL ANALYSIS

A reflection holographic lens is typically exposed by the use of two counterpropagating spherical waves, as shown in Fig. 1. A local Cartesian coordinate system was chosen with the z axis normal to the hologram. The crystal selected for the analysis is a z -cut (c axis perpendicular to the crystal surface) Fe-doped LiNbO₃ crystal. For simplification of the calculation without loss of generality, the point sources i and O are located in the x - z plane an equal distance from the z axis. Another simplification introduced is a local linearity assumption: in a very small region ($\delta x, \delta y$), the interference between two spherical waves is approximated as the interference of two plane waves. The simplification was also used by Syms and Solymar in the analysis of holographic lenses

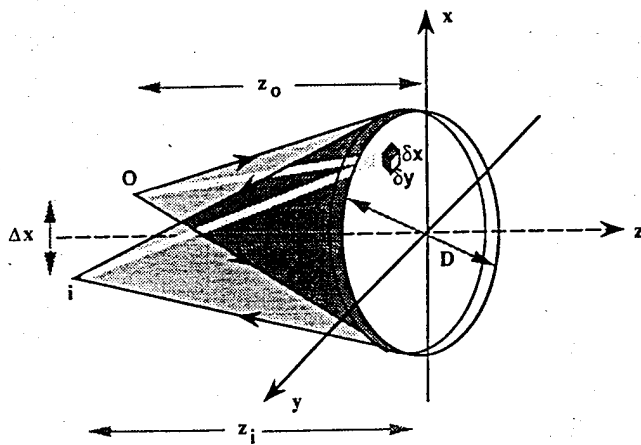
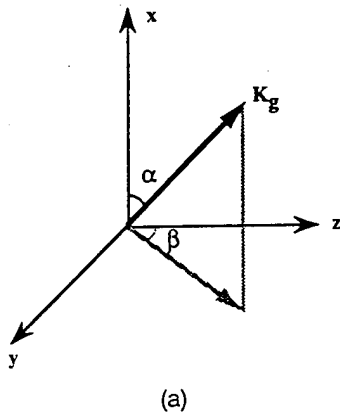
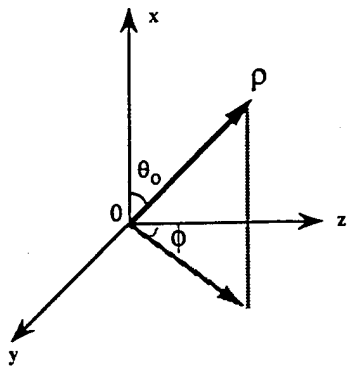


Fig. 1. Three-dimensional description of a reflective volume holographic lens: Δx , off-axis parameter; Z_o , object distance; Z_i , image distance; D , lens aperture.



(a)



(b)

Fig. 2. (a) Orientation of the grating vector K_g . α is the angle between K_g and the x axis, and β is the angle between the z axis and the projection of K_g onto the y - z plane. (b) Orientation of propagation vector ρ of the light beam from source O . θ_o is the angle between ρ and the x axis, and ϕ is the angle between the z axis and the projection of ρ onto the y - z plane.

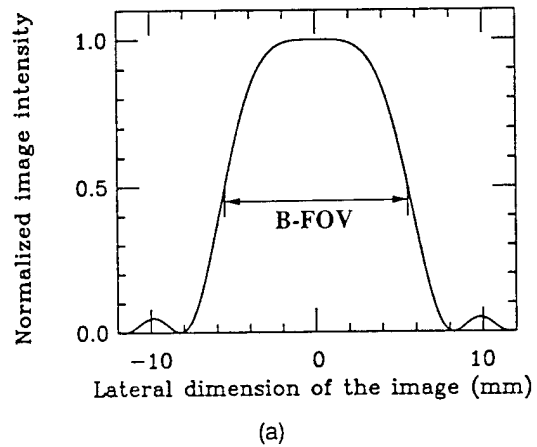
recorded in photographic emulsion¹⁵ and by Latta.¹⁶ The diffraction efficiency of the lens impulse response is simply the integration of the paths of the diffracted wave over the entire crystal aperture:

$$\eta = \left| \frac{1}{\pi R^2} \int_{x^2+y^2=R^2} S(x, y) dx dy \right|^2, \quad (1)$$

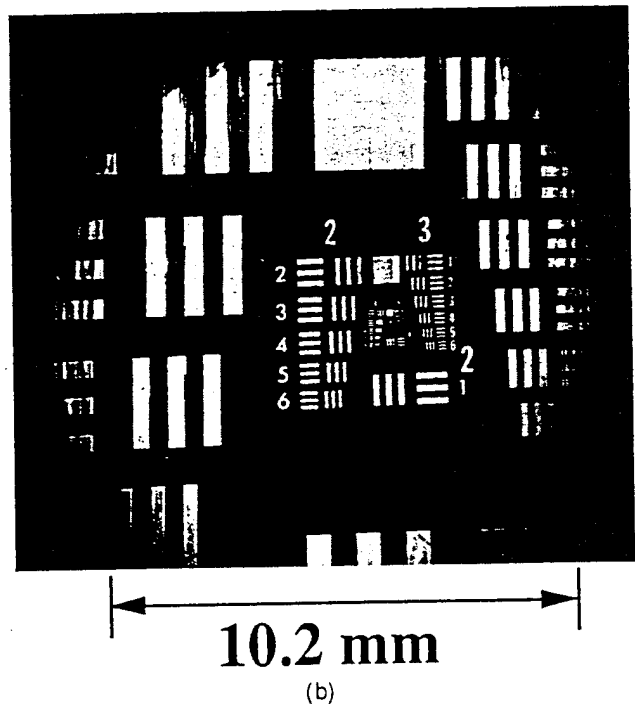
where R is the radius of the holographic lens aperture and $S(x, y)$ is the amplitude of the diffracted wave. We calculated the diffracted wave by using Kogelnik's coupled-wave equations for thick planar holograms¹⁷:

$$S(x, y) = \left(\frac{C_R}{C_S} \right)^{1/2} \left/ \left[j \frac{\xi}{\vartheta} + \left(1 - \frac{\xi^2}{\vartheta^2} \right)^{1/2} \right] \right. \times \coth(\vartheta^2 - \xi^2)^{1/2}, \quad (2)$$

where C_R and C_S are obliquity factors,¹⁷ ξ is related to the dephasing parameter ϑ by



(a)



(b)

Fig. 3. (a) Image intensity distribution of uniform object imaged by a reflective holographic lens recorded in a 1-mm-thick LiNbO₃ crystal. Parameters of lens aperture $D = 2$ cm, $\lambda = 0.514 \mu\text{m}$, off-axis $\Delta x = 0$, and focal length 12 cm ($F/\# 6$) were used in the calculation. The Bragg-limited field of view (B-FOV) is calculated to be 10.4 mm. (b) Image of a resolution target formed by a lens simulated in (a). The measured B-FOV is 10.2 mm.

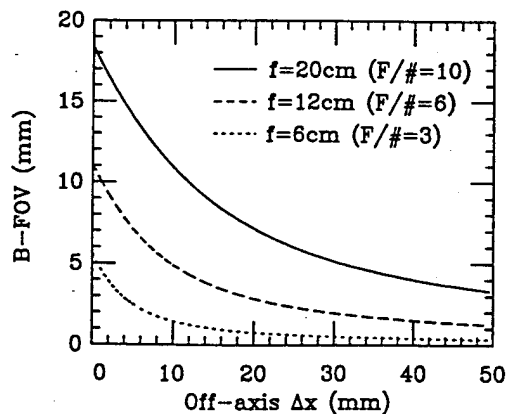


Fig. 4. B-FOV as a function of off-axis parameters for different $F/\#$ (or focal length) lenses recorded in a 1-mm-thick LiNbO_3 crystal. Parameters of $D = 2$ cm and $\lambda = 0.514 \mu\text{m}$ were used in the calculation.

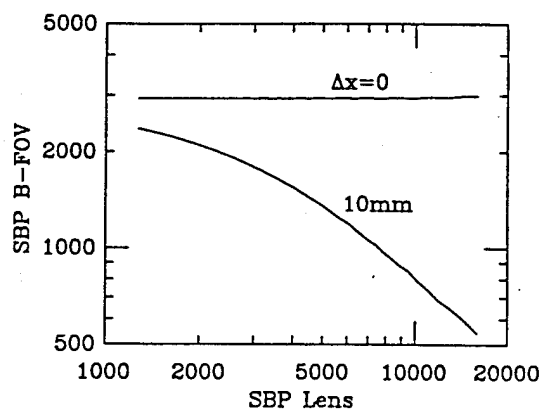


Fig. 5. Relationship between SBP B-FOV and SBP Lens for different off-axis parameters. Parameters of $D = 2$ cm, $d = 1$ mm, and $\lambda = 0.514 \mu\text{m}$ were used in the calculation.

$$\xi = -\frac{\partial d}{2C_S}, \quad (3)$$

$$\vartheta = K_g \cos(\alpha - \theta_o - \Delta\theta) - (\lambda_o + \Delta\lambda) \frac{K_g^2}{4\pi n}, \quad (4)$$

and ϑ is related to the refractive-index modulation Δn by

$$\vartheta = \frac{j\pi\Delta n}{\lambda_o(C_R C_S)^{1/2}}, \quad (5)$$

where d is the crystal thickness, K_g is the magnitude of the grating vector \mathbf{k} , α is the angle between the grating vector \mathbf{k} and the x axis [see Fig. 2(a)], θ_o is the angle between the light beam from source O and the x axis [see Fig. 2(b)] measured inside the material, $\Delta\theta$ is the angular deviation from the Bragg angle during imaging, $\Delta\lambda$ is the wavelength deviation from the recorded wavelength λ_o , and n is the refractive index chosen according to the polarization of the beams. The refractive-index modulation Δn in Eq. (5) is induced by the space-charge field by means of the electro-optic effect.¹⁸ With the light polarization in the y - z plane and the fact that the z component of the space-charge field is much larger than the x and y components, the index modulation recorded in the LiNbO_3 crystal can be expressed as

$$\Delta n = \frac{1}{2}(n_o^3 r_{13} \cos \phi + n_e^3 r_{33} \sin \phi) E_{sc} \sin \alpha \cos \beta, \quad (6)$$

where n_o and n_e are the ordinary and the extraordinary refractive indices, respectively, r_{13} and r_{33} are the electro-optic coefficients, ϕ is the angle between the z axis and the light beam (from source O) projected onto the y - z plane measured inside the material [see Fig. 2(b)], α and β are the orientations of the grating vector [see Fig. 2(a)], and E_{sc} is the amplitude of the space-charge field generated by the optical irradiance. The expression of E_{sc} for photovoltaic media (such as LiNbO_3) derived by Gu et al. based on Kukhtarev's photorefractive theory²⁰ was used in our calculations:

$$E_{sc} = E_q \left\{ \frac{E_{oph}^2 + E_d^2}{[(N_A/N_D)E_{oph}]^2 + (E_d + E_q)^2} \right\}^{1/2}, \quad (7)$$

where N_A and N_D are densities of compensative acceptors and traps, respectively; E_{oph} is the photovoltaic field that is a constant for a given medium; and E_d and E_q are

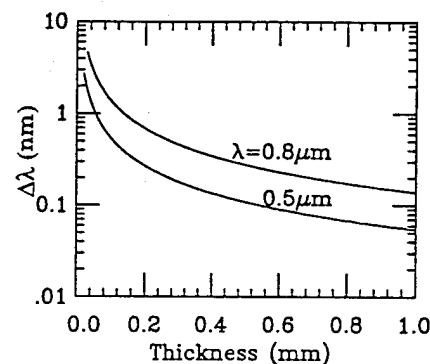


Fig. 6. Wavelength selectivity ($\Delta\lambda$) as a function of crystal thickness for different operating wavelengths. Parameters of $\Delta x = 0$, $D = 2$ cm and $f = 12$ cm ($F/\# 6$) were used in the calculation.

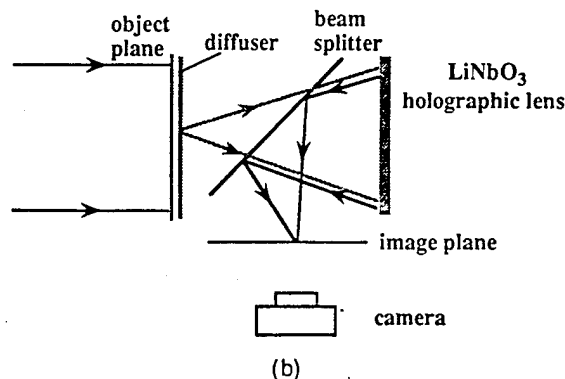
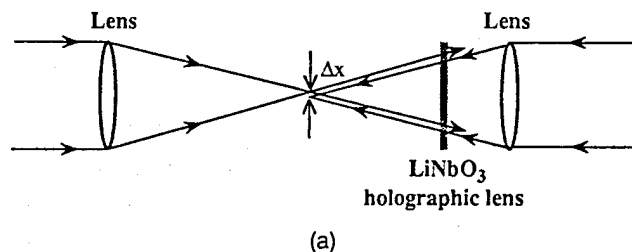
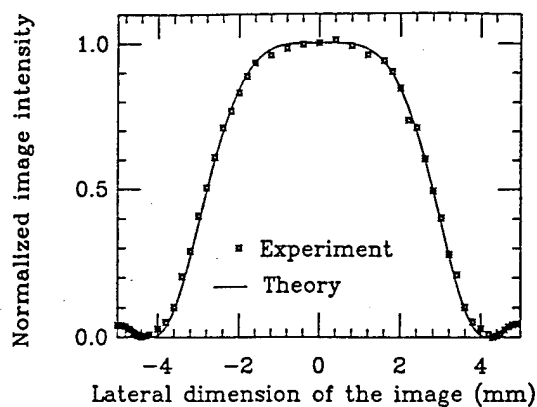
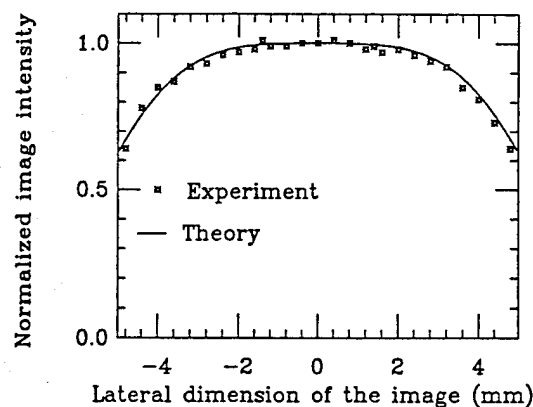


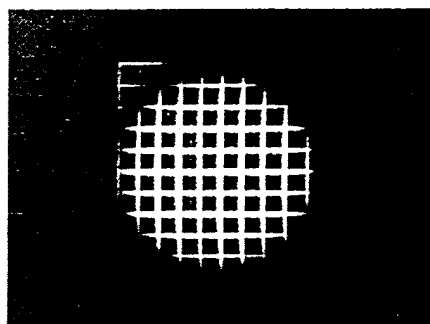
Fig. 7. Optical setup for recording a reflective photorefractive holographic lens; (b) photorefractive lens used to image an object into a camera.



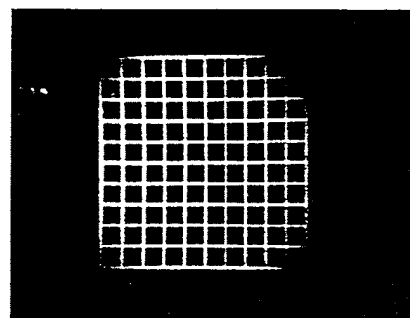
(a)



(c)



(b)



(d)

Fig. 8. Continues on facing page.

the diffusion field and the saturation field, respectively, which depend on the grating period and therefore vary with the x, y coordinate (see Fig. 1) for a grating recorded by two spherical waves. The expressions of E_d and E_q as a function of grating vector K_g are

$$E_d = \frac{k_B T K_g}{e}, \quad (8)$$

$$E_q = \frac{e N_A (N_A - N_D)}{\epsilon K_g N_D}, \quad (9)$$

where k_B is Boltzman's constant, T is the temperature, e is the charge on the electron, and ϵ is the static dielectric constant.

We performed the simulations in the following sections by making use of the LiNbO₃ crystal parameters: $n_o = 2.28$, $n_e = 2.20$, $N_A = 2 \times 10^{16}/\text{cm}^3$, $N_D = 4 \times 10^{17}/\text{cm}^3$, $r_{13} = 9.6 \times 10^{-12}$ m/V, and $r_{33} = 30.9 \times 10^{-12}$ m/V. We used E_{oph} as the only free parameter. Best fits to the experiment of diffraction-efficiency measurement were obtained with $E_{\text{oph}} = 5.6$ kV/cm.

A. Bragg-Limited Field of View

Because of the nature of Bragg angular selectivity in a volume hologram, we expect narrow field of view in imaging with our holographic lenses. A uniform input object consisting of point sources with infinitely small separation will reconstruct a nonuniform output image, as shown in Fig. 3. An on-axis lens (focal length 12 cm, $F/\#$ 6) was

simulated; the result is displayed in Fig. 3(a). The lens was then recorded; Fig. 3(b) shows a photograph of a resolution target imaged through the lens, demonstrating the field of view. As indicated in Fig. 3, the field of an object that can be imaged is limited. Although the effect of Bragg angular selectivity on field of view was discussed by Syms and Solymar,¹⁴ no detailed analysis has been given so far. Instead of the conventional definition of field of view, which measures primarily the effect of vignetting by the lens aperture,²¹ we introduce here a new definition called Bragg-limited field of view (B-FOV), which is useful for characterizing volume holographic lenses. B-FOV measures the effects of the Bragg angular selectivity on the lateral uniformity of the image intensity. We define it to be the lateral dimension of a uniform object that can be imaged with the intensity variation smaller than 50%. As an example, the B-FOV in Fig. 3(a) is calculated to be 10.4 mm: the width of the diffracted image at half of the maximum intensity, which is close to the experimental measurement of 10.2 mm [see Fig. 3(b)]. The B-FOV depends strongly on the lateral separation of the two recording sources (Δx) and f -number ($F/\#$) of the holographic lenses. The $F/\#$ is defined similarly to that of a conventional lens: $F/\# = f/D$, where f is the focal length and D is the lens aperture. However, the dependence of B-FOV on $F/\#$ is mainly through f . The effect of D becomes noticeable only for very small- $F/\#$ lenses, i.e., $F/\# \approx 1$, when the Bragg angle selectivity for the gratings near the aperture and that near the center becomes significantly different.

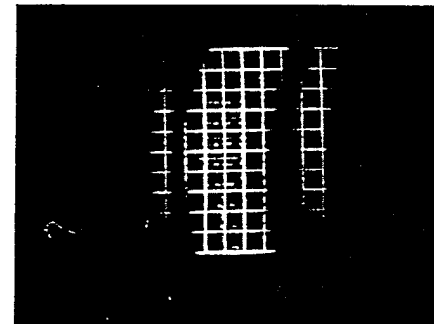
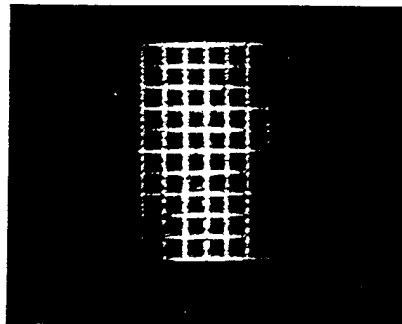
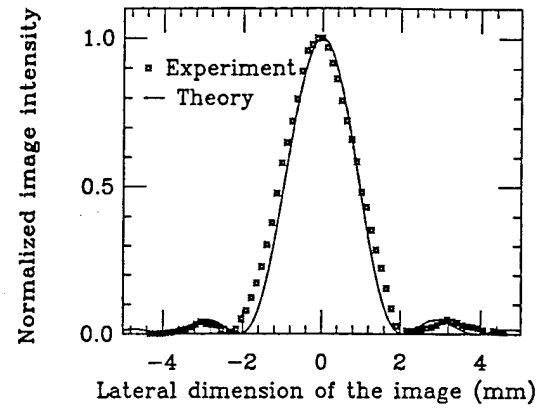
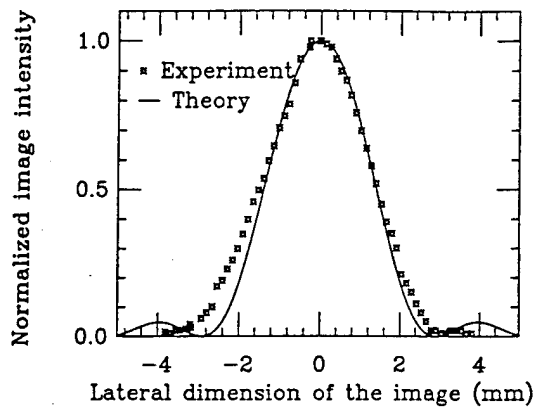


Fig. 8. Experimental and theoretical results of the Bragg angular selectivity on the intensity uniformity of the image formed by volume holographic lenses recorded at different $F/\#$'s and different off-axis parameters Δx : (a) with (b), the corresponding image photograph: on axis ($\Delta x = 0$), $F/\# 3$ ($f = 6$ cm, $D = 2$ cm); (c) with (d), the corresponding image photograph: on-axis ($\Delta x = 0$), $F/\# 6$ ($f = 12$ cm, $D = 2$ cm); (e) with (f) the corresponding image photograph: off-axis $\Delta x = 20$ mm, $F/\# 6$; (g) with (h), the corresponding image photograph: off-axis $\Delta x = 30$ mm, $F/\# 6$. Other parameters such as $d = 1$ mm and $\lambda = 0.514 \mu\text{m}$ were used for both experiment and theory.

We calculated the B-FOV as a function of off-axis parameters for different $F/\#$'s (or focal lengths) by using Eqs. (1)–(9); it is shown in Fig. 4. The calculation was made on the basis of a 1-mm-thick LiNbO_3 crystal with an aperture size of 2 cm and with $\lambda = 0.514 \mu\text{m}$ illumination. The calculation shows that B-FOV drops quickly as the off-axis parameter increases or as the $F/\#$ decreases. This implies that a small- $F/\#$ lens might not be always desirable, since the throughput of the lens is limited not only by the conventional space-bandwidth product (SBP) of the lens but also by the extent of the B-FOV. The B-Fov has a direct effect on the SBP optimization.

B. Space-Bandwidth-Product Optimization

Two figures of merit can aid in the evaluation of the imaging capacity of thick holographic lenses: the SBP of images limited by the lens aperture and the SBP of images limited by the B-FOV. We define the SBP of the B-FOV (SBP B-FOV) and the SBP of the lens (SBP Lens) as

$$\text{SBP B-FOV} = \frac{\text{B-FOV}}{\delta_x}, \quad (10)$$

$$\text{SBP Lens} = \frac{D}{\delta_x}, \quad (11)$$

where $\delta_x = 2 \times 1.22(\lambda f/D)$ is the diffraction-limited spot size. The relationship between SBP B-FOV and SBP Lens is demonstrated by fixing the lens aperture $D = 2$ cm and varying the focal length; the result is shown in Fig. 5. In general, a small- $F/\#$ lens will provide a large SBP Lens but a small SBP B-FOV, and vice versa. The optimum condition for a maximum-image information throughput is that these two parameters be equal. For example, an optimum SBP of 2000 (calculated in one dimension) is obtained in the case of off-axis $\Delta x = 10$ mm, which corresponds to an $F/\# 16$ lens. In the special case $\Delta x = 0$ (on-axis), when focal length (or $F/\#$) decreases, both the B-FOV and the δ_x decrease at the similar rate, resulting in a SBP B-FOV that is almost constant.

C. Wavelength Selectivity

Although the B-FOV is strongly dependent on Δx and $F/\#$, the wavelength selectivity $\Delta\lambda$ of the lens is almost independent of these parameters. The latter is much more strongly dependent on crystal thickness and operating wavelength. Figure 6 shows the wavelength selectivity ($\Delta\lambda$) as a function of crystal thickness at operating wavelengths of 0.8 and 0.5 μm . The wavelength selectivity is defined to be the minimum change in wavelength required for recording two lenses without cross talk. For $\lambda = 0.8 \mu\text{m}$, $\Delta\lambda$ decreases from 1.4 to 0.14 nm when the

thickness increases from 100 μm (a maximum thickness that can be obtained from nonphotorefractive materials) to 1 mm. On the other hand, for a 1-mm-thick lens, $\Delta\lambda$ decreases from 0.14 to 0.06 nm when λ changes from 0.8 to 0.5 μm . The wavelength selectivity in volume holographic lenses is very similar to that of volume planar gratings, which is approximately given by

$$\Delta\lambda = \frac{\lambda_o^2}{nd \sin \varphi}, \quad (12)$$

where φ is the half-angle between the two recording beams measured inside the material.

3. EXPERIMENTS ON LENS CHARACTERIZATION

A. Bragg-Limited Field of View

The optical system for recording reflective holographic lenses is shown in Fig. 7(a). The spherical waves used for recording the lenses were generated by two conventional achromatic optical glass lenses. The holographic lenses were recorded in a 1-mm-thick LiNbO_3 crystal (0.05% Fe doping) with an Ar laser operated at $\lambda = 0.514 \mu\text{m}$. The B-FOV of the recorded lens was evaluated with use of the imaging configuration shown in Fig. 7(b); a diffuser was placed in front of the object for analysis, and a beam splitter was used to reflect the image plane into the detector (or camera). The purpose of using a diffuser in B-FOV measurement is to make the experimental conditions as close as possible to the theoretical calculations, which assumed that the object is an array of point sources. A plane wave was used as an object in B-FOV measurement, and a detector covered by a pinhole (0.1 mm in diameter) detected the variation of diffraction efficiency with different locations on the image by laterally scanning across the image. The measured diffraction efficiency as a function of lateral position in the image plane is shown in Fig. 8. Figures 8(a) and 8(c) show the simulation and measurement of B-FOV for on-axis ($\Delta x = 0$) lenses of $F/\# 3$ ($f = 6 \text{ cm}$ and $D = 2 \text{ cm}$) and $F/\# 6$ ($f = 12 \text{ cm}$ and $D = 2 \text{ cm}$), respectively. Figures 8(e) and 8(g) show the results of $F/\# 6$ lenses with off-axis parameters of 20 and 30 mm, respectively. The data points show excellent agreement with the theoretical predictions. The diffraction efficiency measured at the center of the image was 17%. Figures 8(b), 8(d), 8(f), and 8(h) show the corresponding output images of a 10-mm \times 10-mm grid input. For on-axis lenses [Figs. 8(a)–8(d)] the B-FOV is symmetrical in both the horizontal and the vertical directions. However, for off-axis lenses [Figs. 8(e)–8(h)] the B-FOV is restricted more in the horizontal direction, the direction of off-axis shift of the two recording waves; and the B-FOV in the vertical direction is similar to that of the on-axis lenses. The region at which the reconstruction is strongest is not rectangular [see Fig. 8(h)] because of Bragg degeneracy during imaging.

B. Resolution

We measured near-aperture-limited diffraction performance for the reflection lenses. Figure 9 shows the mea-

surement system. An on-axis lens ($F/\# 3$) recorded in a 1-mm-thick LiNbO_3 crystal was used to image a resolution target. The image formed by the photorefractive lens was then magnified and imaged to a camera by an $F/\# 2$ conventional glass lens. Figure 10(a) shows the total view ($\sim 5.8 \text{ mm}$ in diameter) of the image without the use of the magnification lens; Fig. 10(b) shows the optically magnified center portion of the image of Fig. 10(a) produced when a magnification lens was used. Here group 6, element 4, or 5.5 μm , can be resolved. The theoretical prediction of aperture-limited diffraction resolution is 3.8 μm .

C. Wavelength Selectivity

For measuring the wavelength selectivity of the photorefractive lenses, an argon pumped Ti-sapphire tunable laser operated at near infrared was used. Figure 11 shows the experimental data and the theoretical prediction of normalized diffraction efficiency versus wavelength tuning $\Delta\lambda$. $\Delta\lambda = 0.15 \text{ nm}$ was obtained in a 1-mm-thick lens recorded in a LiNbO_3 crystal at $\lambda = 0.8 \mu\text{m}$. This highly wavelength-selective nature of the reflection hologram was also employed by Yariv et al. in constructing a holographic color filter.²² This small $\Delta\lambda$ will allow us to multiplex more than 150 holographic lenses, using a tunable semiconductor laser diode (external cavity) with a wavelength-tuning range of 25 nm.

4. APPLICATION DEMONSTRATIONS

Photorefractive lenses may find several important applications as a result of their unique properties, such as high wavelength selectivity, which permits the superposition of many lenses in the same volume; *in situ* recording for self-alignment; low weight; simplicity of fabrication; and potentially low manufacturing cost.

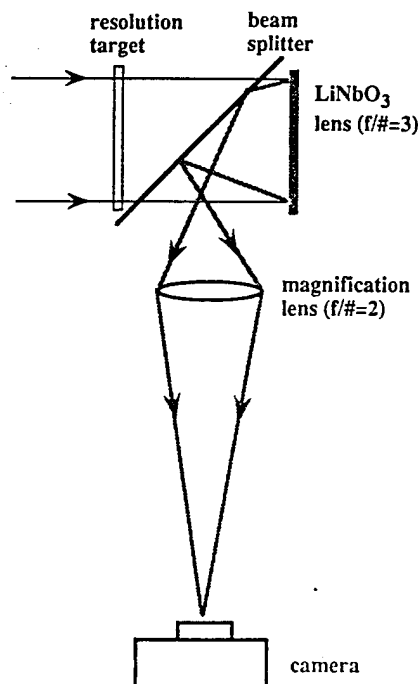


Fig. 9. Experimental setup for resolution measurements

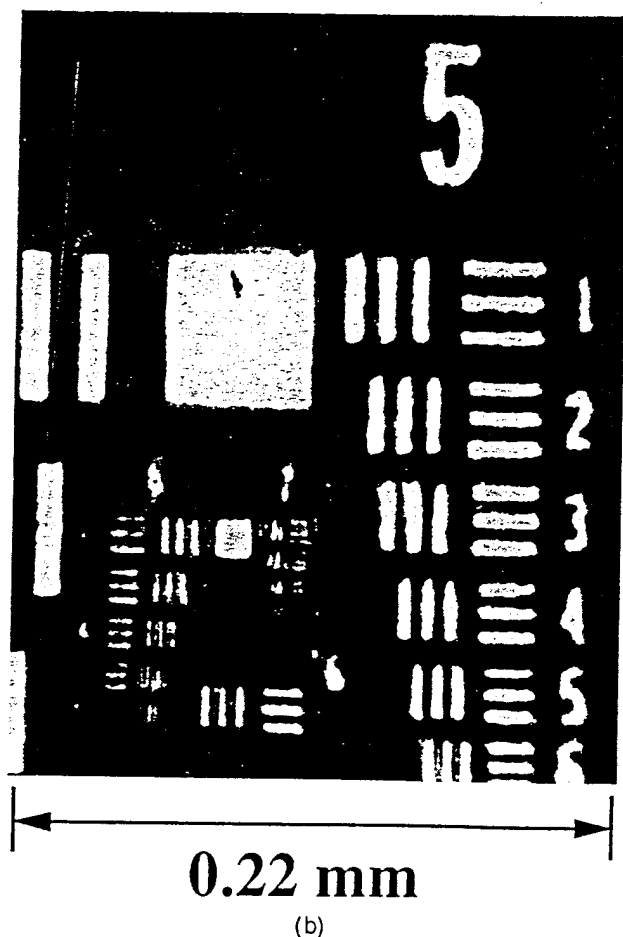
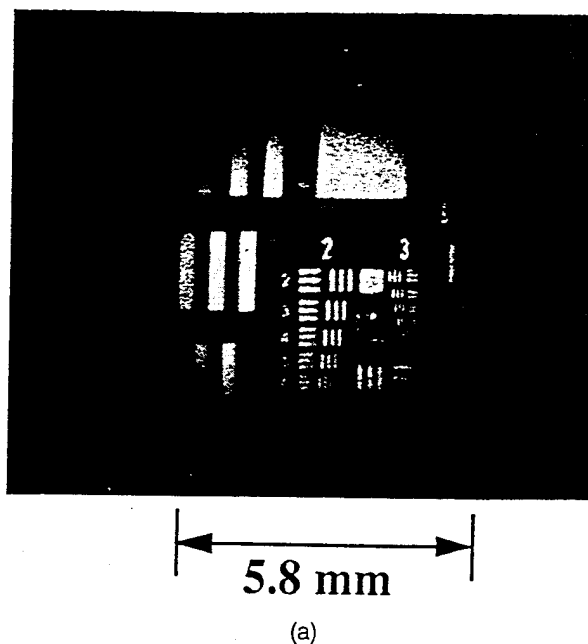


Fig. 10. Image of a resolution target formed by an $F/\# 3$ photorefractive lens: (a) global view of the image, (b) partial view of the image magnified by a magnification lens. Group 6-4 ($5.5 \mu\text{m}$) can be resolved.

Two examples demonstrated in Subsections 4.A and 4.B show the use of the property of wavelength multiplexing to achieve dynamic focusing and dynamic lateral image shifting without mechanical movement.

A. Dynamic Focusing without Mechanical Movement
In the first application we demonstrate that dynamic focusing in an imaging system can be achieved with the use of wavelength-multiplexed photorefractive lenses. Different object planes can be selected merely by tuning of the wavelength without the use of mechanical movement. In the experiment, two lenses for imaging two

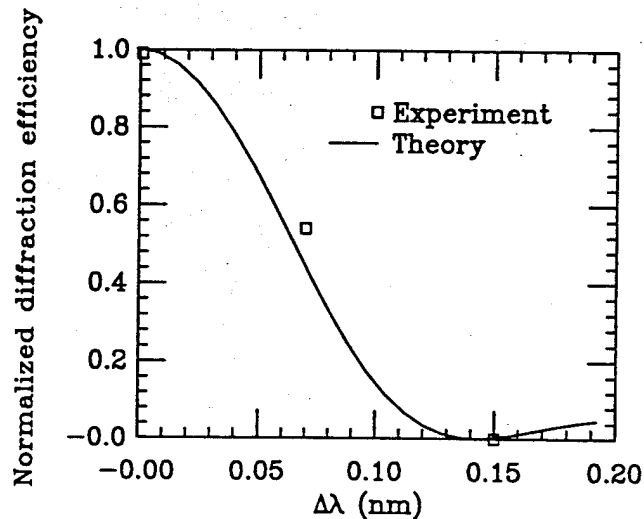


Fig. 11. Experimental result and theoretical calculation of the wavelength selectivity obtained for a 1-mm-thick reflective photorefractive lens of $f = 12 \text{ cm}$ ($F/\# 6$) recorded at $\lambda = 0.8 \mu\text{m}$.

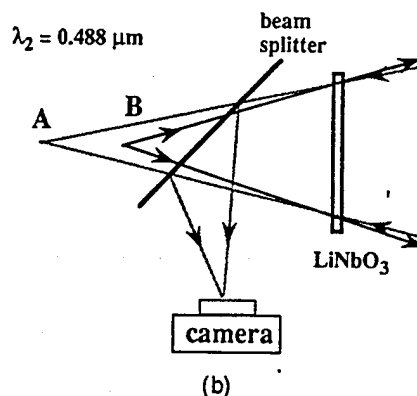
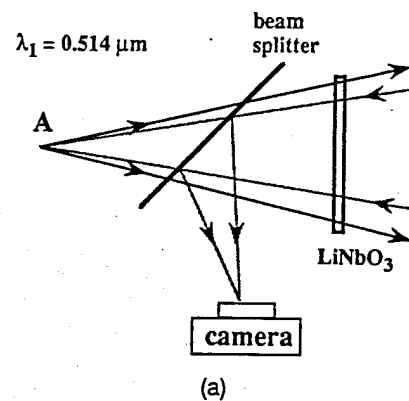


Fig. 12. Schematic diagram for multiplexing (recording) two lenses of different object distances for dynamic focusing: (a) object at position A with imaging at the camera plane recorded at $\lambda_1 = 0.514 \mu\text{m}$, (b) object at position B with imaging at the camera plane recorded at $\lambda_2 = 0.488 \mu\text{m}$.

objects of different longitudinal distances were superimposed in a 1-mm-thick LiNbO_3 crystal with use of two lines of an Ar laser, 0.514 and 0.488 μm . Figure 12 shows the schematic diagram for recording. The first lens, with the object plane at position A, 100 mm from the crystal, and the image plane with a camera at a distance of 100 mm from the crystal [Fig. 12(a)], was recorded with $\lambda_1 = 0.514 \mu\text{m}$. The second lens, with the object plane at position B, 67 mm from the crystal, but with the same image position as that of the first lens [Fig. 12(b)], was recorded with $\lambda_2 = 0.488 \mu\text{m}$. The exposure times were controlled according to the recording schedule²³ so that the diffraction efficiencies of the two lenses were similar ($\eta \approx 5\%$). The two superimposed lenses were then used for the dynamic focusing demonstration. First, a grid pattern was placed at position A and a diffuser was placed in front of the object. When the object was illuminated by the wrong wavelength (i.e., $\lambda_2 = 0.488 \mu\text{m}$), the image was completely defocused [Fig. 13(a)]. However, when the wavelength was tuned to its correct value (i.e., $\lambda_1 = 0.514 \mu\text{m}$), the image was perfectly focused, as shown in Fig. 13(b). Next, the object was moved from the A to the B position, and the corresponding wavelength for perfect focusing was also switched, from 0.514 to 0.488 μm , as shown in Figs. 13(c) and 13(d) (no diffuser was used in this case). The image was magnified by a factor of 1.5 as a result of the difference between object and image distances. Figures 13(a) and 13(c) show

the difference in the image properties produced when an object is illuminated by a diffuse source and by a plane wave.

B. Lateral Image Shifting without Mechanical Movement

In the second application example we demonstrate lateral scanning of an input, using wavelength-multiplexed photorefractive lenses. Two lenses were multiplexed with different wavelengths (0.514 and 0.488 μm , respectively) in the same volume. The recording scheme is shown in Fig. 14. These two lenses were different in lateral object positions instead of in longitudinal object positions (as in the first example). During imaging, an input of two characters (U and C) constructed with 50- μm pixels [Fig. 15(a)] was placed in the object plane, and a camera was placed in the image plane. An iris was used that allowed only one of the characters to be imaged into the camera. When the object was illuminated by $\lambda_1 = 0.514 \mu\text{m}$, the U and the C were shifted by the lens so that only the U was imaged onto the camera [Fig. 15(b)]. When $\lambda_2 = 0.488 \mu\text{m}$ was used for illumination, the U and the C were shifted by a second lens so that only the C was imaged onto the camera [Fig. 15(c)]. Because the undesired images [e.g., the letter C in Fig. 15(b) and the letter U in Fig. 15(c)] were shifted outside the camera (or detector plane), cross talk was not an issue.

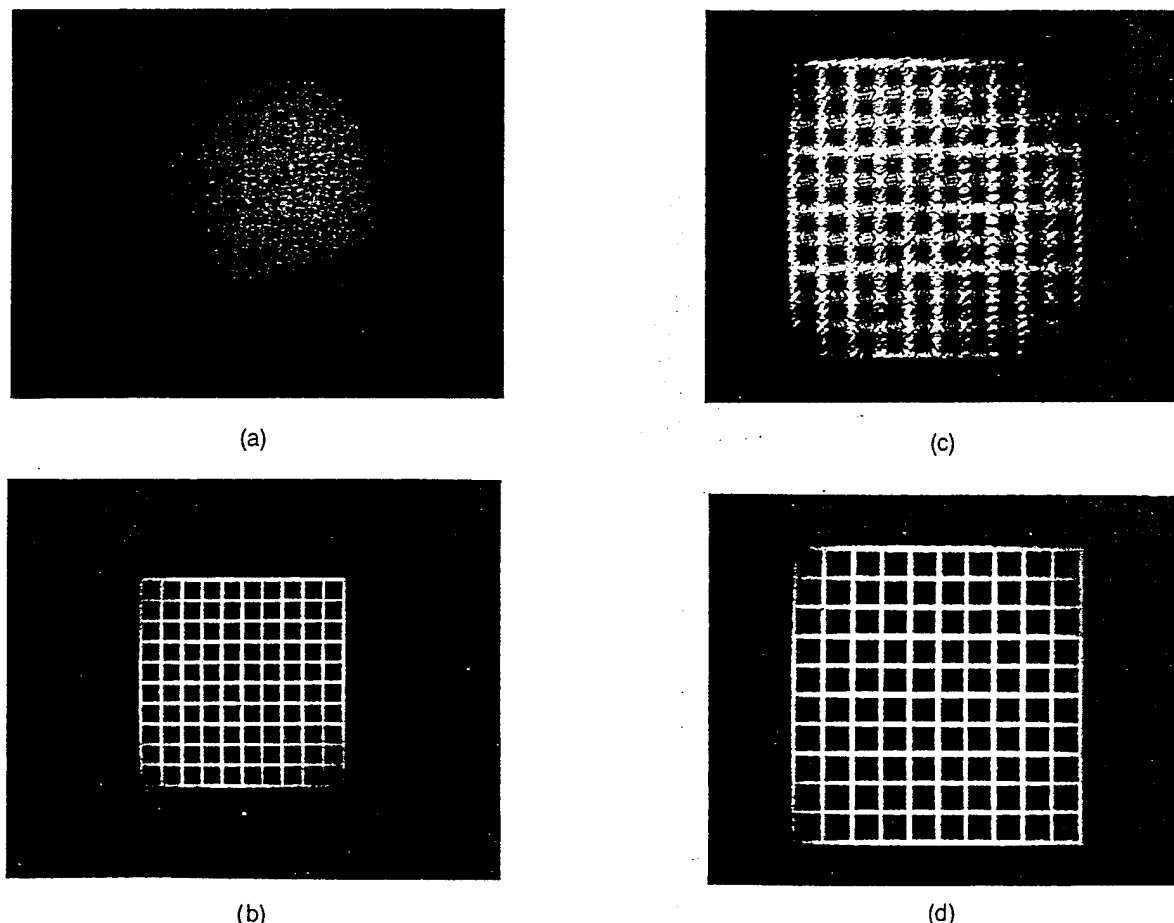


Fig. 13. Experimental result of dynamic focusing: image obtained by placement of the object at position A (see Fig. 12), illuminated by (a) $\lambda_2 = 0.488 \mu\text{m}$ and (b) $\lambda_1 = 0.514 \mu\text{m}$; image obtained by placement of the object at position B (see Fig. 12), illuminated by (c) $\lambda_1 = 0.514 \mu\text{m}$ and (d) $\lambda_2 = 0.488 \mu\text{m}$.

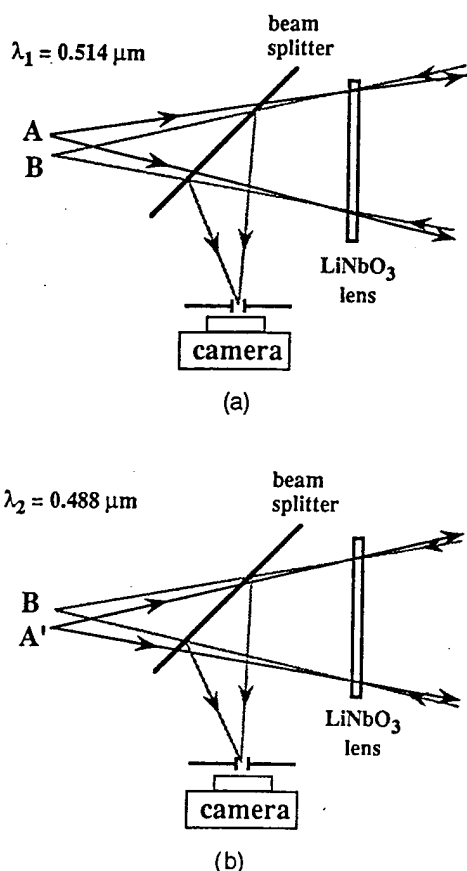


Fig. 14. Schematic diagram for multiplexing (recording) two lenses of different object lateral positions for dynamic image shifting: (a) object at position A, image at position B, recorded at $\lambda_1 = 0.514 \mu\text{m}$; (b) object at position A', image at position B, recorded at $\lambda_2 = 0.488 \mu\text{m}$.

5. DISCUSSION

Two important issues relevant to practical applications are energy efficiency and the availability of a wavelength-tunable source.

The energy loss that results from the use of a beam splitter can be resolved easily by the use of a polarization beam splitter, PBS, and a quarter-wave ($\lambda/4$) plate, as shown in Fig. 16. The p -polarized input object beam passing through PBS and the $\lambda/4$ plate becomes a circularly polarized beam when it strikes the LiNbO₃ lens. The reconstruction from the reflection holographic lens passes through the $\lambda/4$ plate and is then s polarized, being reflected toward the image plane. The diffraction efficiencies of the linear polarized beam and the circular polarized beam are similar, because the hologram recorded in the z -cut LiNbO₃ lens is not sensitive to polarization.

The holographic lens efficiency is strongly dependent on the number of superimposed lenses. The effective index modulation for each hologram is $\Delta n_s/N$, where Δn_s is the saturation refractive-index modulation and N is the number of superimposed holograms. For example, a single lens was measured to have an efficiency of 50%. However, when 10 lenses are superimposed ($N = 10$), the diffraction efficiency falls to 0.8%, and for 100 lenses the diffraction efficiency is 0.008%. The illumination power and the detector sensitivity, combined with the hologram efficiency, ultimately determine the number of scanning

positions that can be implemented by a single crystal. The diffraction efficiency can be enhanced by the use of other materials or by an increase in the crystal thickness, but there will be a corresponding change in the field of view.

Currently available tunable sources include external cavity laser diodes. Although the tuning range is quite large ($>50 \text{ nm}$), the tuning is mechanical and inherently

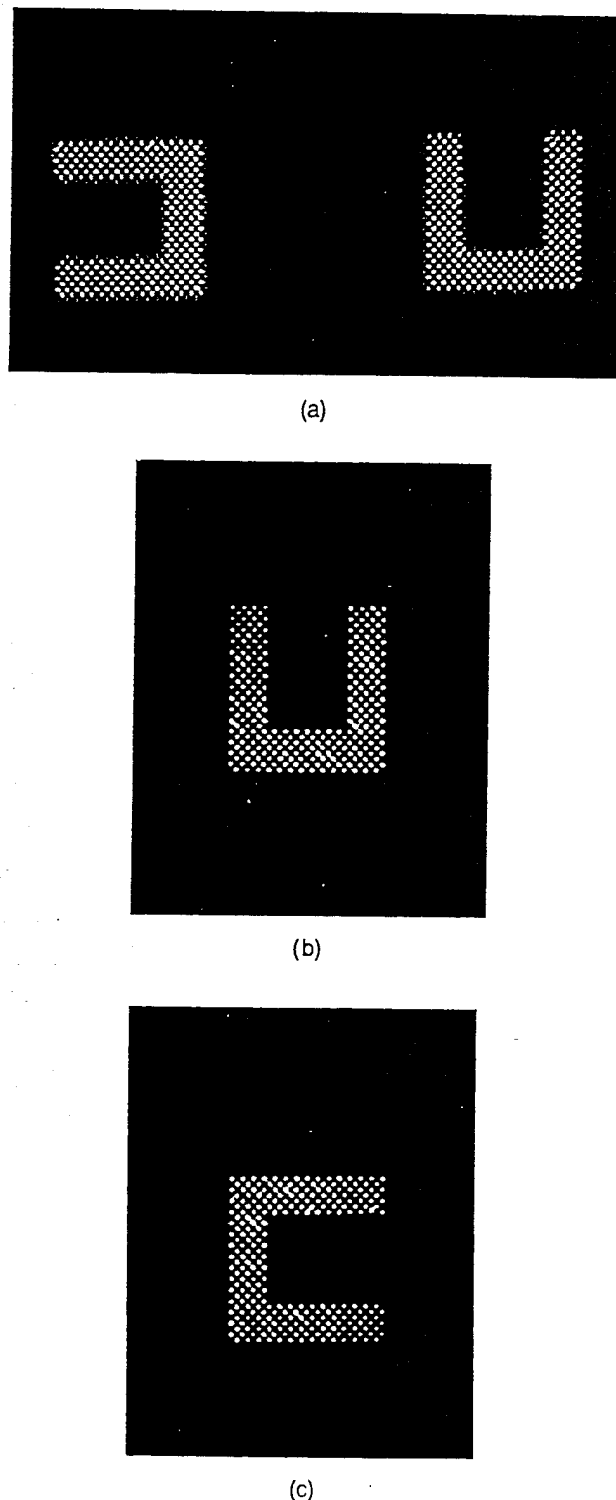


Fig. 15. Experimental result of dynamic image lateral shifting: (a) input object (pixel size $50 \mu\text{m}$), (b) output image obtained at $\lambda_1 = 0.514 \mu\text{m}$, (c) output image obtained at $\lambda_2 = 0.488 \mu\text{m}$.

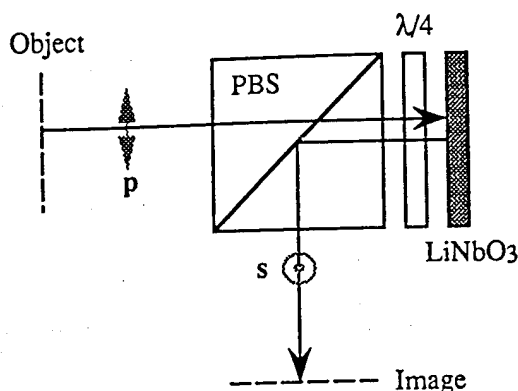


Fig. 16. Energy loss resulting from the use of a beam splitter can be reduced by the use of a polarization beam splitter and a quarter-wave plate.

slow. However, several integrated electronically tunable laser diode sources are under development. For example, Chang-Hasnain *et al.*²⁴ have demonstrated a surface emitting diode laser array capable of continuously tuning at a rate of 660 ns/nm. In addition, Schilling *et al.*⁹ have demonstrated a discrete laser diode capable of selecting one of twelve discrete wavelengths at a rate of 1 GHz.

6. CONCLUSION

In this paper we have reported results of design, modeling, experiments, and prototyping applications of volume reflection holographic lenses. We demonstrated that a simple ray-tracing model incorporating photorefractive physics can be used to model 1-mm-thick holographic lenses with an arbitrary $F/\#$. We defined a new figure of merit, the Bragg-limited field of view, that describes the sizes of images reconstructed from volume holographic lenses. When comparing this figure of merit with the diffraction-limited resolution of various lenses, we observed that there are optimal designs for reflection holographic lenses. We verified the model by conducting experiments in a photorefractive LiNbO_3 crystal, and the results were an excellent fit to the prediction. We demonstrated as potential applications the multiplexing of two reflection holographic lenses for imaging different longitudinal and transversal planes. In one case dynamic focusing was explored. In the second case lateral image scanning was achieved. As demonstrated in this paper, volume holographic materials can provide sufficient storage to hold several multiplexed lenses with narrow spectral bandwidths and useful fields of view.

ACKNOWLEDGMENTS

This research was supported by the U.S. Office of Naval Research under grant N00014-91J-1618. A preliminary version of this research was presented at the Optical Society of America 1992 annual meeting.²⁵

REFERENCES

1. S. Hunter and S. C. Esener, "Holographic dynamic focusing lens for volume optical memory applications," in *Photonics for Computers, Neural Networks, and Memories*, S. T. Kowel, W. J. Miceli, and J. A. Neff, eds., Proc. Soc. Photo-Opt. Instrum. Eng. **1773**, 15–23 (1992).
2. T. J. Drabik and S. H. Lee, "Shift-connected SIMD array architectures for digital optical computing systems, with algorithms for numerical transforms and partial differential equations," *Appl. Opt.* **25**, 4053–4064 (1986).
3. S. T. Kowel, P. Kornreich, and A. Nouhi, "Adaptive spherical lens," *Appl. Opt.* **23**, 2774–2777 (1984).
4. Y. Nishimoto, "Variable-focal-length lens using an electro-optic effect," U.S. patent 4,466,703 (August 21, 1984).
5. T. Tatebayashi, T. Yamamoto, and H. Sato, "Electro-optic variable focal-length lens using PLZT ceramic," *Appl. Opt.* **30**, 5049–5055 (1991).
6. A. W. Lohmann, "What optics can do for the digital optical computer," in *Optical Computing*, Vol. 5 of OSA 1985 Technical Digest Series (Optical Society of America, Washington, D.C., 1985), paper TuA1.
7. W. Kulcke, K. Kosanke, E. Max, H. Fleisher, and T. J. Harris, "Convergent beam digital light deflector," in *Optical and Electro-optical Information Processing*, J. T. Tippet, D. A. Berkowitz, L. C. Clapp, C. J. Koester, and A. Vanderburgh, Jr., eds. (MIT Press, Cambridge, Mass., 1965), pp. 371–418.
8. Y. Fainman and S. H. Lee, "Advances in applying nonlinear optical crystals to optical signal processing," in *Signal Processing Handbook*, C. H. Chen, ed. (Dekker, New York, 1988).
9. M. Schilling, W. Idfer, E. Kühn, G. Laube, H. Schweizer, Künstel, and O. Hildebrande, "Integrated interferometric injection laser: novel fast and broad-band tunable monolithic light source," *IEEE J. Quantum Electron.* **27**, 1616–1623 (1991).
10. E. N. Leith and J. Upatnieks, "Zone plate with aberration correction," *J. Opt. Soc. Am.* **57**, 699 (1967).
11. Y.-Z. Liang, D. Zhao, and H.-K. Liu, "Multifocus dichromated gelatin hololens," *Appl. Opt.* **22**, 3451–3456 (1983).
12. A. W. Lohmann and F. Sauer, "Holographic telescope arrays," *Appl. Opt.* **27**, 3003–3007 (1988).
13. M. R. Latta and R. V. Pole, "Design techniques for forming 488-nm holographic lenses with reconstruction at 633 nm," *Appl. Opt.* **18**, 2418–2421 (1979).
14. R. R. A. Syms and L. Solymar, "Effect of angular selectivity on the monochromatic imaging performance of volume holographic lenses," *Opt. Acta* **30**, 1303–1318 (1983).
15. R. R. A. Syms and L. Solymar, "Experimental and theoretical evaluation of the efficiency of an off-axis volume holographic lens," *Appl. Phys. B* **32**, 165–173 (1983).
16. J. N. Latta, "Computer based analysis of hologram imagery and aberrations. I. Hologram types and their nonchromatic aberration," *Appl. Opt.* **10**, 599–608 (1971).
17. H. Kogelnik, "Coupled wave theory for thick hologram gratings," *Bell Syst. Tech. J.* **48**, 2909–2947 (1969).
18. See, for example, A. Yariv and P. Yeh, *Optical Waves in Crystal* (Wiley Interscience, New York, 1984), Chap. 7.
19. C. Gu, J. Hong, H.-Y. Li, D. Psaltis, and P. Yeh, "Dynamics of grating formation in photovoltaic media," *J. Appl. Phys.* **69**, 1167–1172 (1991).
20. N. V. Kukhturev, V. B. Markov, S. G. Odulov, M. S. Soskin, and V. L. Vinetskii, "Holographic storage in electrooptic crystals. I. Steady state," *Ferroelectrics* **22**, 949–960 (1979).
21. See, for example, E. Hecht, *Optics*, 2nd ed. (Addison-Wesley, Reading, Mass., 1990), Chap. 5.
22. A. Yariv, G. Rakuljic, and V. Leyva, "Comparison of angle and wavelength multiplexing in holographic data storage," in *Annual Meeting*, Vol. 23 of OSA 1992 Technical Digest Series (Optical Society of America, Washington, D.C., 1992), p. 102.
23. D. Psaltis, D. Brady, and K. Wagner, "Adaptive optical networks using photorefractive crystals," *Appl. Opt.* **27**, 1752–1759 (1988).
24. C. J. Chang-Hasnain, L. T. Florez, J. P. Harbison, and M. W. Maeda, "Two-dimensional multiple wavelength tunable surface-emitting laser array," in *Annual Meeting*, Vol. 17 of OSA 1991 Technical Digest Series (Optical Society of America, Washington, D.C., 1991), p. 37.
25. J. Ma, B. Catanzaro, Y. Fainman, and S. H. Lee, "Reflection volume holographic lenses with wide field of view and wavelength multiplexing," in *Annual Meeting*, Vol. 23 of OSA 1992 Technical Digest Series (Optical Society of America, Washington, D.C., 1992), p. 189.

Appendix D

Photorefractive Lens Array Image System Design Optimization

The memory distribution network interconnect, as originally described, had no explicit restriction on the relative size of the lenses and sub-fields of memory. Depending on their relative sizes, the interconnect can be characterized as either similar to a space-variant interconnect or similar to a space-invariant interconnect. If it were more space-invariant, the number of lenses would be few, if it were more space-variant, the number of lenses would be large. Given the characteristics of imaging with volume holographic lenses described elsewhere, it becomes apparent that there are both diffractive effects and geometrical optics effects that impact the design of this interconnect. Therefore one expects that there is some tradeoff between the number of pixels that can be imaged through the system and the degree of space-variance of the interconnect.

To study this tradeoff, several optical systems were simulated. Using the analytic results described previously for the diffractive optics effects, it was possible to determine the aperture limited spot size and the Bragg limited field of view. Using CodeV™ the effects of astigmatism on the PSF and the imaging field distortion could be analyzed. The lens array was assumed to be fabricated in 1 mm thick LiNbO₃. The wavelength of operation was 800 nm. Several systems were studied by changing the size of the lenses and the distance off-axis of the image. The criteria for measuring the performance of these systems will be the density of SBWP.

The density of SBWP is essentially the number of resolvable points that can be transmitted through the system in a certain area:

$$\text{SBWP Density} = \frac{\text{SBWP}_{\text{Lens}}}{A_{\text{Lens}}}, \quad (\text{D.1})$$

In this equation, $\text{SBWP}_{\text{Lens}}$ refers to the SBWP that can pass through each lens in the interconnect and A_{Lens} refers to the area of each lens. In this way, the system with the highest communication density can be identified.

One method to calculate the SBWP that can be imaged by the lenses of the interconnect is to evaluate the point spread function of each lens and to determine the size of the largest image that can be faithfully imaged by the lens. The SBWP that can be imaged by a lens in this configuration can be defined as:

$$SBWP_{Lens} = \frac{\Delta}{\delta}. \quad (D.2)$$

Geometric and diffractive effects contribute to both the spot size (δ) and the image size (Δ). The overall spot size was taken to be the square root of the sum of the squares of the geometric and diffractive spot sizes:

$$\delta = \sqrt{\delta_g^2 + \delta_d^2}. \quad (D.3)$$

To determine the maximum size of the undistorted image due to distortion, we chose the minimum of volume holographic lens field of view and the distortion limited field of view. Combining this with the area of the lens, A_{Lens} , we can calculate our original figure of merit (Eqn D.1) the SBWP density.

Tables **D1** and **D2** show data for the density of the SBWP for interconnects with various size lenses recorded at 800 nm in 1 mm thick lithium niobate (index of refraction = 2.28). The data is organized in the following way: Table **D1** shows data for the case where the F/# of the lenses in the array is kept constant and Table **D2** includes data for the case where the focal length of the interconnect remains constant. Two parameters are varied in the comparisons. The lens diameter is varied to indicate the degree of space variance of the lens array interconnect. The off-axis distance (the distance between the center image and the center of the lens) is also varied. In these tables, the off-axis distance is expressed as the multiple of the diameter of the lens. For instance, an off-axis distance of $5D$ for a lens diameter of 2 mm is 10 mm.

When the F/# is fixed (Table **D1**), larger aperture lenses demonstrate a much higher capability for transmitting high density data. Aberrations and distortions are not very great except when the off-axis distance becomes large. In this situation, the larger lenses demonstrate a much higher capacity for transmitting high density data. However, with this large F/#, the optical system can be quite large. The focal length of the system was fixed in order to explore the tradeoffs with various F/#'s (Table 2). Here, for small lenses, the diffraction limit prohibits the transmission of high density data. For large lenses, the low F/# causes severe aberrations affecting both the spot size and the image field size. As a result, a moderate lens size of 2 mm demonstrates the best performance for a variety of off-axis imaging distances.

Lens Diameter	Off-Axis Distance: 0	Off-Axis Distance: D	Off-Axis Distance: 2D	Off-Axis Distance: 5D
0.2 mm	39	39	21	3
0.5 mm	244	244	126	15
2 mm	3906	3811	1700	96
5 mm	24414	20006	6901	103

Table D. Density of SBWP for different lens diameter with fixed F/#

Lens Diameter	Off-Axis Distance: 0	Off-Axis Distance: D	Off-Axis Distance: 2D	Off-Axis Distance: 5D
0.2 mm	0	0	0	0
0.5 mm	15	15	15	5
2 mm	3906	3811	1700	96
5 mm	152588	511	23	0

Table D2 Density of SBWP for different lens diameter with $f = 40$ mm fixed

Appendix E
Wavelength-multiplexed Reconfigurable Interconnect
using a Volume Holographic Lens Array

Wavelength-multiplexed reconfigurable interconnect using a volume holographic lens array

B. Cantanzaro, J. Ma, Y. Fainman, and S. H. Lee

Department of Electrical and Computer Engineering, University of California, San Diego, La Jolla, California 92093-0407

Received March 16, 1994

Wavelength-multiplexed holograms have been used to store $\log(N)$ stages of an N -node butterfly interconnect. We recorded and reconstructed the holograms, using LiNbO_3 over a range of 790 to 800 nm. The wavelength separation can be as little as 0.6 nm between holograms. We implemented the interconnect by recording a 4×4 array of elements that contained five superimposed lenses each. These lenses formed a semi-space-variant optical interconnect with a space-bandwidth product larger than 2×10^3 for each $2 \text{ mm} \times 2 \text{ mm}$ lens.

Optical interconnection has been advocated as a means for achieving highly parallel, wide-bandwidth interconnects.¹ Optical interconnects can be constructed as multistage interconnection networks (MIN's) to provide wide-diameter networks with reduced contention and fault tolerance. In this Letter we present an experimental demonstration of a wavelength-multiplexed holographic lens array designed for a MIN that uses a single stage of optics.

The most straightforward method of constructing an optoelectronic MIN is to arrange the hardware in a series of optical interconnect and electronic processing layers.² Such a system can be fully pipelined and have a large throughput. However, with this technique there is a large hardware cost and power requirement (optical as well as electronic). In addition, the alignment difficulties in constructing and packaging this type of system grow significantly with the number of stages. One alternative to this technique is to use a single optical interconnect and electronic processing layer and to take the output of that single stage iteratively and send it through the input of that same stage until the desired routing is achieved.³ By using the large storage capacity of volume holograms, one can multiplex and store several stages of a MIN in a single holographic optical element. With the appropriate optics,⁴ the output of the interconnect can be fed back into input of the interconnect. By reconfiguring the interconnect by playing back each successive stage of the optical interconnect, one can implement a MIN with a single stage of optics and electronics. Using wavelength multiplexing for addressing the holograms has become more realistic with recent advances in tunable laser diode technology⁵ and infrared holography.⁶ Sparse arrays of these tunable laser diodes can be used as part of a spatial light modulator to provide inputs for a wavelength-multiplexed optical interconnect. The advantage of the multiplexing approach is a great reduction in system volume, hardware cost, alignment tolerances, and instantaneous power consumption. There is, of course, a price to be paid for this approach: an increase in the illumination source complexity and the loss of the ability to pipeline the network.

The optical system used to demonstrate our reconfigurable interconnect is diagrammed in Fig. 1. The vertically polarized input image enters a polarizing beam splitter and reflects toward a quarter-wave plate. The image is then right-hand circularly polarized when it strikes the holograms in lithium niobate. Because reflection holograms are recorded with the c axis perpendicular to the surface in lithium niobate, the holograms are insensitive to polarization. The reflection from the holograms then passes through the quarter-wave plate and is horizontally polarized, allowing it to pass through the beam-splitter and be imaged to a CCD camera.

The reflection holograms were an array of holographic lenses recorded in a 1-mm-thick sample of lithium niobate (0.1% iron mole by weight, argon annealed); a separate automated exposure system with a tunable titanium:sapphire laser was used. The lithium niobate was then placed into the reconstruction system with the aid of a kinematic mount. The multiplexed holograms consisted of an array of 16 separate elements, $2 \text{ mm} \times 2 \text{ mm}$ in size. Each element further contains five wavelength multiplexed on- and off-axis lenses ($f = 40 \text{ mm}$) that image portions of the input plane to different areas in the output plane. Illuminating the input with a set of wavelengths permits access to different lenses and reconfiguration of the interconnect pattern.

A well-known interconnect used for both routing and computation, the butterfly network, was chosen for demonstration. An N -node butterfly has $\log(N)$ interconnection stages. For the $N = 16$ implementation, we recorded the four stages along with a straight-through interconnection, using different wavelengths. To demonstrate the interconnect, we prepared a mask with a set of 16 numbers indicating the positions of each mode in the interconnect. This input was imaged through the optical interconnect stage, and the results were captured by a CCD camera. Figure 2 shows photographs of the outputs of the successive stages in the network. To demonstrate clearly the interconnection at each stage, we used the same input for all: the ordered array of numbers shown in Fig. 2(e).

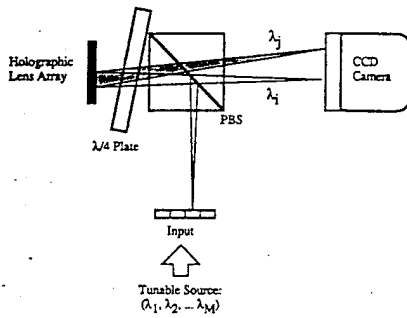
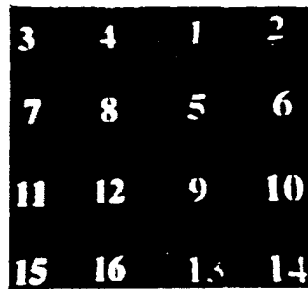


Fig. 1. Optical system for implementing a reconfigurable semi-space-variant interconnect.

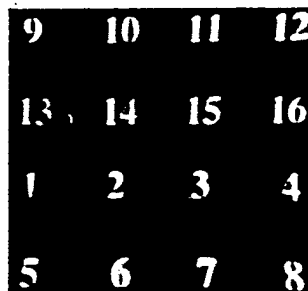
The performance of the holographic lens array may be evaluated with four parameters: the maximum off-axis imaging distance, the space-bandwidth product (SBWP) imaged by each lens, the wavelength separation required for reconfiguration, and the insertion loss. The field of view⁷ of photo-refractive lenses determines the off-axis imaging distance. Given our optical system, a field of view of $2 \text{ mm} \times 2 \text{ mm}$ (the size of the lens elements) can be maintained for as much as 6.4 mm off axis (3 nodes to each side, 48 nearest neighbors). We determined the SBWP imaged by each lens by measuring the resolution and the field of view. The resolution

can be defined by the Raleigh criteria as the full width at half-maximum of the point-spread function, which was measured to be $38 \mu\text{m}$ (compared with a diffraction limit of $32 \mu\text{m}$). For a lens aperture of $2 \text{ mm} \times 2 \text{ mm}$, each lens could resolve 2×10^3 pixels, and the array of 16 lens elements could resolve a SBWP of larger than 4×10^4 . We achieved close wavelength spacing between holograms by using a 1-mm thick reflection hologram.⁸ The holograms in this study have demonstrated selectivities of 0.15 nm (equal to that predicted by Kogelnik) in the near infrared. Cross talk was less than -23 dB . The actual minimum separation between stored holograms (0.6 nm) in this system was limited by the modes of the laser, not by hologram cross talk. The insertion loss in this interconnect is determined by the saturation diffraction efficiency and the number of stored interconnects. At saturation the insertion loss is -3.7 dB , yielding a theoretical insertion loss of -16 dB for multiplexing five holograms. In this experiment the insertion loss was measured to be -20 dB .

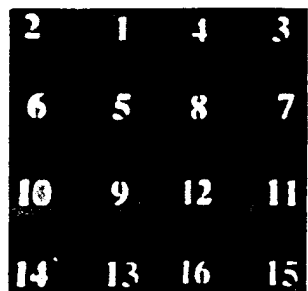
The scalability of the lens array is controlled by two important factors: the SBWP imaged by the lenses and the diffraction efficiency of the volume hologram. Under the assumptions of large- f -number lenses and diffraction-limited resolution, the maximum SBWP



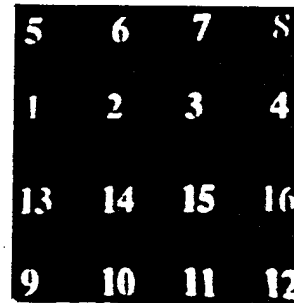
(a)



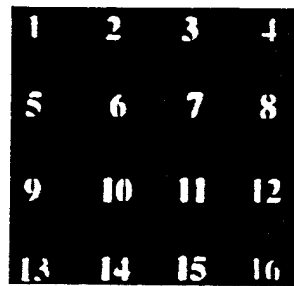
(b)



(c)



(d)



(e)

Fig. 2. (a) Vertical half-fold (stage 1: $\lambda = 799.8 \text{ nm}$), (b), horizontal half-fold (stage 2: $\lambda = 796.6 \text{ nm}$), (c) vertical quarter-fold (stage 3: $\lambda = 801.1 \text{ nm}$), (d) horizontal quarter-fold (stage 4: $\lambda = 798.2 \text{ nm}$), (e) straight-through interconnect (stage 5: $\lambda = 798.8 \text{ nm}$).

imaged by each lens can be calculated to be

$$\text{SBWP} = \left(\frac{2nf_H D_H}{\delta d} \right)^2, \quad (1)$$

where n is the index of refraction, f_H is the focal length of the lenses in the array, D_H is the size of the aperture of the lens, δ is the largest distance that the lens must image off axis, and d is the thickness of the holographic substrate. For the present design, holographic lens arrays of greater than 10^3 elements can be fabricated, each with the capability of imaging 2×10^3 pixels each. However, these lenses can image only to 48 of their nearest neighbors because of the field-of-view limitation in the holographic lenses. Clearly, the diameter of the interconnect can be increased at the sacrifice of the bandwidth imaged by the lenses.

The number of holograms that can be multiplexed (in each position in the array) is limited by the insertion loss of the system. Using an approximation to Kogelnik's results for diffraction efficiency yields the following insertion loss:

$$\begin{aligned} \text{Loss} &= \text{Diffraction efficiency} + \text{absorption} \\ &= 20 \log_{10} \left(\frac{\pi \Delta n_{\text{sat}} L}{\lambda} \right) \text{dB} - 20 \log_{10}(m) \text{dB} \\ &\quad - \alpha L \log_{10}(e) \text{dB} \\ &= 1.28 \text{ dB} - 20 \log_{10}(m) \text{dB}. \end{aligned} \quad (2)$$

In Eq. (2) $\Delta n_{\text{sat}} = 2.2 \times 10^{-4}$ (the saturation index), $L = 1$ mm (the crystal thickness), m is the number of holograms multiplexed in each location of the array, $\alpha = 2.3 \text{ cm}^{-1}$ (the absorption of lithium niobate), and $\lambda = 0.8 \text{ }\mu\text{m}$ (the wavelength of illumination). For

the storage of 25 interconnections in each lens position ($m = 25$), the wavelength range necessary for reconfiguration is only 3.75 nm, but the insertion loss is -27 dB.

In conclusion, we offer an alternative to standard methods of constructing optoelectronic MIN's: multiplexed holographic interconnects. This technique reduces system volume as well as optical and electronic hardware costs. An optical interconnect was demonstrated with five stages stored in a single stage of optics with access to each stage by illumination with different wavelengths. The system was operated at near-infrared wavelengths and with a close separation between wavelengths to show its compatibility with laser diode technology.

References

1. H. Arsenault, T. Szoplik, and B. Macukow, *Optical Processing and Computing* (Academic, Orlando, Fla., 1989), Chap. 1.
2. A. Krishnamoorthy, P. Marchand, F. Kiamelev, and S. C. Esener, *Appl. Opt.* **31**, 5480 (1991).
3. S. H. Lin, T. F. Krile, and J. F. Walkup, *Proc. Soc. Photo-Opt. Instrum. Eng.* **752**, 209 (1987).
4. B. Catanzaro, J. Ma, Y. Fainman, and S. H. Lee, *Proc. Soc. Photo-Opt. Instrum. Eng.* **2152**, 154 (1994).
5. M. Scholling, W. Idler, E. Kühn, G. Laube, H. Schweizer, K. Wüstel, and O. Hildebrand, *IEEE J. Quantum Electron.* **27**, 1616 (1991).
6. B. Catanzaro, J. Ma, Y. Fainman, and S. H. Lee, in *Annual Meeting*, Vol. 23 of 1992 OSA Technical Digest Series (Optical Society of America, Washington, D.C., 1992), p. 112.
7. J. Ma, B. Catanzaro, J. E. Ford, Y. Fainman, and S. H. Lee, *J. Opt. Soc. Am. A* **11**, 2471 (1994).
8. G. A. Rakuljic, V. Leyva, and A. Yariv, *Opt. Lett.* **17**, 1471 (1992).

Appendix F

Memory Distribution Network System Description

The memory distribution network segment that was constructed had to obey certain constraints that defined the architecture. There were constraints from the optical components, the electronic components, as well as their integration.

The optical system was constrained by several practical considerations. The majority of the design constraints were discussed in previously. Aside from these theoretical limits, there were several more pragmatic considerations. The material for the volume holographic lenses was only available in thickness between 0.5 mm to 5 mm, impacting the field of view and the diffraction efficiency of the element. The wavelength of operation was constrained by both the material and the laser source. Although material demonstrated the fastest time response at shorter wavelengths, the output power of the laser was at a maximum at 810 nm. Maximizing the amount of optical power to the MIP chip would increase the speed of operation. A compromise of 790-800 nm was sought in order to reduce recording times and yet maintain reasonable diffraction efficiency of the hologram.

The electronic MIP chip was also forced to obey certain limitations. The size of the chip was limited to less than a 4 mm x 4 mm area due to cost. The decision to use 2 micron MOSIS, CMOS fabrication was also determined by cost. The detector was based on previous designs of a pre-charged photodiode cell. There exists a tradeoff between the speed of a detector and its sensitivity. Typically, the larger the area of the detector, the more photons can be used to generate carriers for detection and the more sensitive the detector becomes. However, this increase in size increases both the capacitance and the physical transit time of the carriers, reducing the speed. Based on this, the detector size using this CMOS technology is between 10 and 100 microns. In order to achieve faster response time, the detector was designed to be used with a pulsed optical source. The design used a pre-charge pulse that created a voltage across the photodiode just prior to the expected optical pulse. When the optical pulse arrived, it would cause the voltage across the diode to dissipate to ground. The available laser source was not easily pulsed. As a result, lower sensitivity was expected. In addition to the photodetector being sensitive to light, the entire chip's surface would be sensitive, to some degree, to light. The sensitivity of the surrounding logic was close to 0.3 times the sensitivity of the detector. If light with three times the amount of the minimum detectable power was

incident on a transistor, it would cause a false reading for that detector and its nearest neighbors. This would impact the alignment of the chip and the optical interconnect by cause false responses when the chip was mis-aligned. To establish a light-blocking layer to protect the active logic on the chip would have required extensive modifications. It was sufficient to merely place the detectors a reasonable distance away from the logic (one or two diameters of the detector).

The combination of the electronic chip and the optical interconnect created additional constraints on the system. The detector size determined the F/# of the imaging system to be used (assuming diffraction limited performance):

$$10 \text{ microns} \leq \delta \leq 100 \text{ microns}$$

$$12.5 \leq F/\# \leq 125$$

where δ is the diameter of the detector. From the results of the study of SBWP density through semi-space variant interconnects, the range of sizes for the lens has a lower bound of 1 mm; the upper bound is set by the maximum area of less than 4 mm x 4 mm of the chip:

$$1 \text{ mm} \leq D \leq 4 \text{ mm}$$

Within these constraints, a few systems were analyzed based on the volume of the optical system, the number of MIP elements possible in the array and the number of sub-fields of memory each MIP can view using the interconnect. (see Tables F1-F4)

From this manual partitioning of the relative sizes of the electronic and optical components, withing the constraints laid out previously, some conclusions can be drawn. Increasing the detector size has the advantage of allowing for a larger MIP array and greater access to the memory page. However, the cost paid for this is in the volume of the optical system and in the speed of the detectors. Increasing the lens size accomplishes little improvement in performance. However, reducing the size of the object with respect to the size of the lens allows for greater access to the memory page while sacrificing very little. The tradeoff is not apparent in this table, but the reduction of the object size directly reduces the number of pixels (SBWP) that can be transmitted through each lens. However, this limit is already constrained in the MIP plane by the allowable density of detectors.

The final configuration (see Table F5) of the memory distribution network was chosen based on these observations and the availability of optics for recording lenses in the automated exposure system. The MIP element was designed to receive an 8 x 8 array of input pixels on a 125 μm pitch.

The system was constructed using a tunable Ti:Sapphire laser, a fixed input memory page, the lens array, the MIP chip, an LV/500 chip tester to communicate with the MIP chip, and a 486-33 MHz PC to act as the processing element. The PC controlled the wavelength of the illumination source; it could request sub-fields of the memory by changing the wavelength and accessing pre-stored lenses in the interconnect. The PC also controlled the LV/500 chip tester which was used to read the data from the MIP chip.

The PC controlled the system via synchronous, serial communication. It performed all the necessary handshaking between the wavelength tuning and the subsequent reception of data from the LV/500. The role of the LV/500 was to provide the precise timing necessary to operate the chip. This included the pre-charge pulse discussed in previously as well as the addresses necessary to read the values on the detectors. The LV/500 required both hardware and software configuration. Fortunately, this device could be interfaced to a PC via the serial port therefore central control of the system was provided by the PC.

The opto-electronic system is diagrammed in Figure F1 and a photograph of the actual system is included in Figure F2. The input to the system was an optical memory page, represented on an emulsion plate. This was illuminated by the Ti:Sapphire source and the object propagated towards the polarization optics and hologram mount. As mentioned previously, the hologram was mounted on a kinematic mount in order for it to easily moved between the recording system and the interconnect. The kinematic mount was affixed to the same mount that held the polarization optics (beam splitter and quarter-wave plate). The optical distance between the hologram and the object was 80 mm. By virtue of using a unity magnification imaging system for the interconnect, the distance between the chip and the hologram was also 80 mm. The chip was mounted on a translation and rotation stage as was the input. In essence, the hologram and polarization optics were fixed and the other two components were aligned to it. The chip was connected with the LV/500 by using a standard 50-pin ribbon cable (sufficient for low speed operations).

Detector Size	F/#	Lens Diameter	Object Size	Focal Length	Volume per MIP	Number of MIP's	Number of Viewable Sub-Fields
10 μm	12	2 mm	2 mm	12 mm	200 mm ³	150	1
25 μm	31	2 mm	2 mm	31 mm	500 mm ³	975	1
50 μm	62	2 mm	2 mm	62 mm	1000 mm ³	3900	49
100 μm	125	2 mm	2 mm	125 mm	2000 mm ³	15000	841

Table F1. Architecture variations for different detector sizes

Detector Size	F/#	Lens Diameter	Object Size	Focal Length	Volume per MIP	Number of MIP's	Number of Viewable Sub-Fields
25 μm	31	1 mm	1 mm	15 mm	62 mm ³	975	1
25 μm	31	2 mm	2 mm	31 mm	500 mm ³	975	1
25 μm	31	3 mm	3 mm	46 mm	1600 mm ³	975	1
25 μm	31	4 mm	4 mm	62 mm	4000 mm ³	975	1

Table F2. Architecture variations for different lens sizes

Detector Size	F/#	Lens Diameter	Object Size	Focal Length	Volume per MIP	Number of MIP's	Number of Viewable Sub-Fields
25 μm	31	2 mm	0.25 mm	31 mm	500 mm ³	975	225
25 μm	31	2 mm	0.5 mm	31 mm	500 mm ³	975	49
25 μm	31	2 mm	1 mm	31 mm	500 mm ³	975	9
25 μm	31	2 mm	2 mm	31 mm	500 mm ³	975	2

Table F3. Architecture variations for different object sizes

Detector Size	F/#	Lens Diameter	Object Size	Focal Length	Volume per MIP	Number of MIP's	Number of Viewable Sub-Fields
32 μm	40	2 mm	1 mm	40 mm	640 mm ³	1600	25

Table F4. Final system configuration

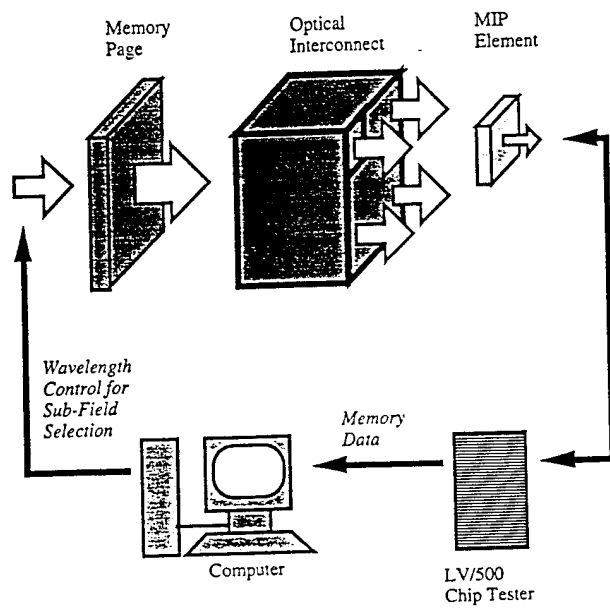


Fig.F1. Block diagram of the experimental memory distribution network.

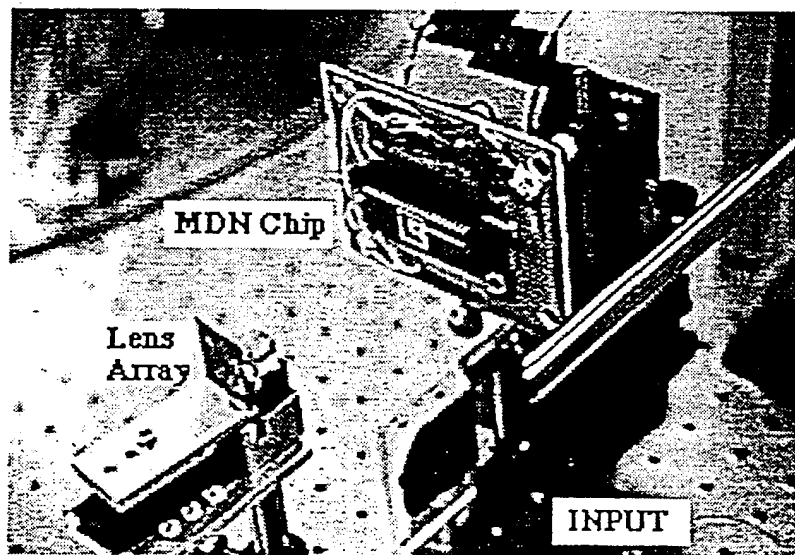


Fig.F2. Photograph of the memory distribution network system.

Appendix G

Application Demonstration - Parallel Data Base Search

Using the MDN prototype system, we have demonstrated how to use a large array memory distribution network to implement a parallel search through an optical memory. For this demonstration, a high resolution emulsion plate was used as the memory page. The memory page consisted of a 4 x 4 array of sub-fields. Each sub-field contained 64 bits of information. Four lens arrays (4 x 4) were multiplexed in the material at separate wavelengths to create four separate interconnects to redistribute the memory. Because the chip could only view a single sub-field of memory, the output of the interconnect was captured using a CCD camera to view the redistribution of the entire memory page, while the chip was used to view and capture and retransmit a single sub-field.

The data for this demonstration was chosen to illustrate how this type of system might be used to search airline flight data for travel agents. The sub-field was divided four segments: the name of the airline company, the destination of the flight, the departure time, and the arrival time. (see Figure G1) Airline data for flights out of San Diego to New York City was compiled and encoded on a memory page (Fig.G2).

The interconnect designed to access this information was based on dividing up the memory page into blocks of memory (4 sub-fields) that could be rapidly searched using the reconfiguring interconnect and the MIP chip. The interconnect allowed a single MIP chip to sequentially access four sub-fields of memory by changing the wavelength of illumination and accessing one of the four holograms stored in each location in the lens array. By distributing different queries to each element in a block (4 MIP chips), the memory page can be scanned in parallel. Figure G3 illustrates the permutations of the interconnect. Four lens arrays were designed, recorded, and aligned to realize these permutations.

The results of this interconnection pattern are illustrated in Figure G4. The entire memory page is shown in each stage of the interconnect. The MIP chip was aligned to the upper-right corner of the lower-left block. The input to the chip for each wavelength is shown in Figure G5. The PC, acting as a processing element connected directly to the MIP, would request a sub-field of memory by tuning the wavelength of the Ti:Sapphire laser source, thereby reading out the appropriate holographic interconnect. The information from the MIP would then be transmitted to the PC via the LV/500. The

software on the PC could be programmed to search for any of the attributes of the field (destination, airline, departure, or arrival information). Figure G6 shows the software interface for controlling the laser wavelength, receiving the MIP chip transmission, and searching the database for an entry matching a query. In this case, the PC was searching for a flight landing in JFK airport.

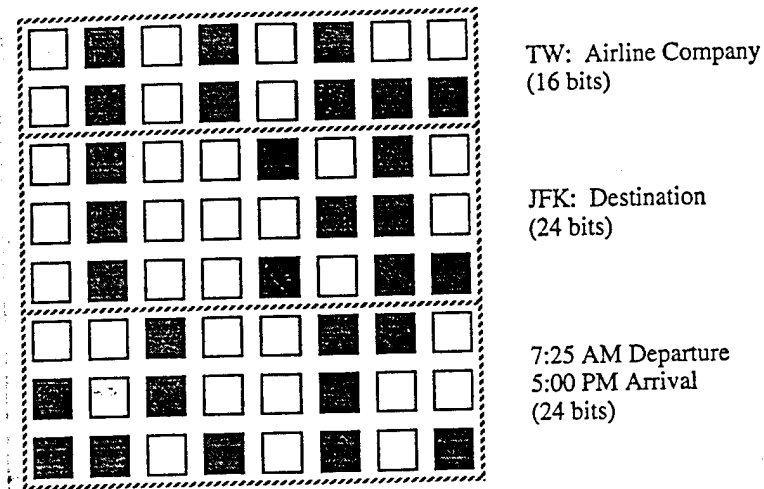


Fig.G1. Sub-field memory organization: 64 bits per sub-field containing airline flight information.

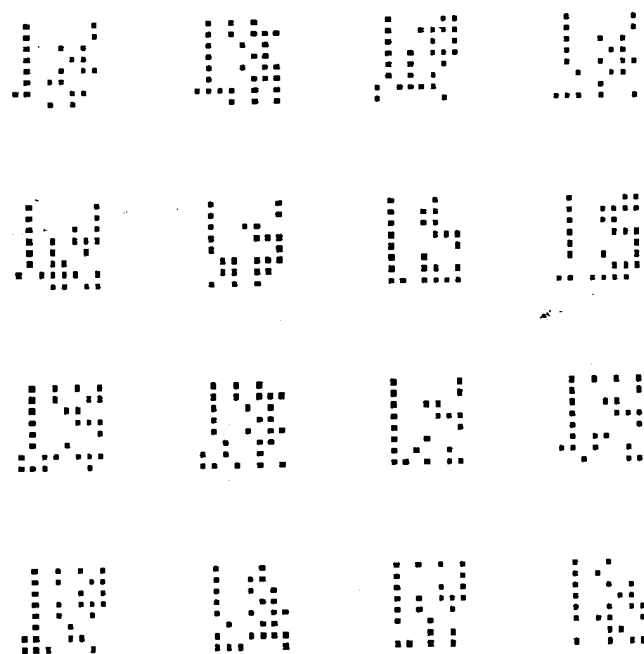


Fig.G2. Entire memory page of encoded airline data.

Original Configuration of the
Memory Page: λ_1

A	B	A	B
C	D	C	D
A	B	A	B
C	D	C	D

Cycle Counter Clockwise: λ_3

B	D	B	D
A	C	A	C
B	D	B	D
A	C	A	C

Cycle Clockwise: λ_2

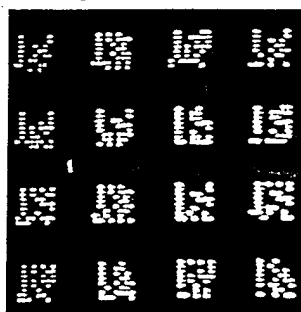
C	A	C	A
D	B	D	B
C	A	C	A
D	B	D	B

Exchange Diagonals: λ_4

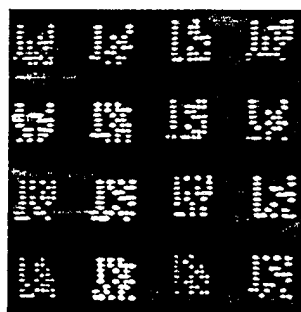
D	C	D	C
B	A	B	A
D	C	D	C
B	A	B	A

Fig.G3. The memory page was further divided into blocks (bold outlines). Inside a single block a MIP (white cell) would be able to access all the information in that block.

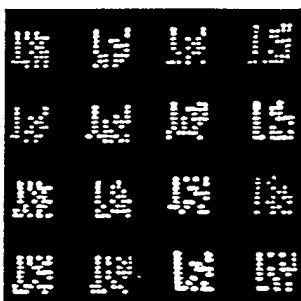
Original Configuration



Cycle Clockwise



Cycle Counter Clockwise



Exchange Diagonals

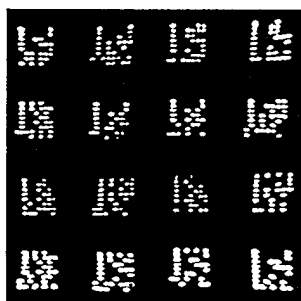


Fig.G4. Four configurations of the interconnect used to demonstrate parallel search of a page oriented memory.

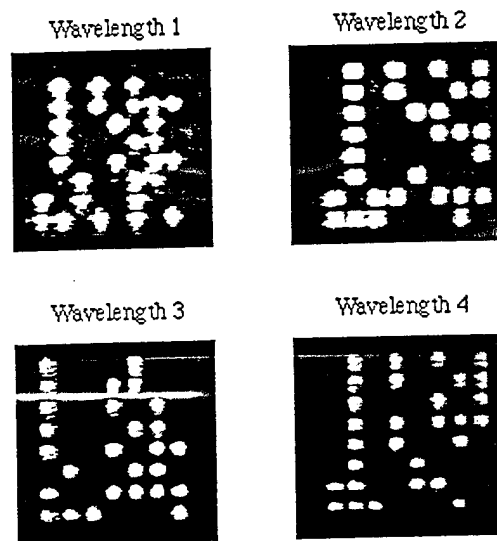


Fig.G5. Data input to the MIP chip located in the upper-right corner of the lower-left memory block shown in Fig.G2.

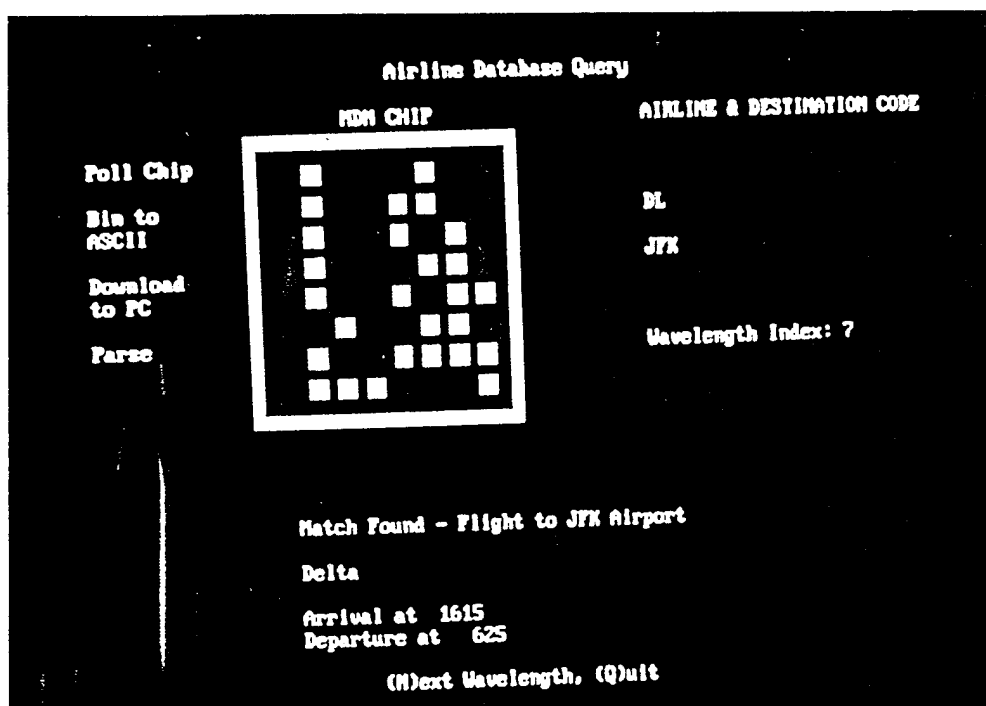


Fig.G6. Software on PC to control the laser wavelength, receive the MIP chip transmission, and search entries in the database.